



CFD INVESTIGATION OF THE FLOW DYNAMICS INSIDE A SPHERICAL SURFACE INDENTATION

THESIS

Robert C. Vincent, 2d Lt, USAF

AFIT/GAE/ENY/06-M31

DEPARTMENT OF THE AIR FORCE
AIR UNIVERSITY

AIR FORCE INSTITUTE OF TECHNOLOGY

Wright-Patterson Air Force Base, Ohio

APPROVED FOR PUBLIC RELEASE; DISTRIBUTION UNLIMITED.

The views expressed in this thesis are those of the author and do not reflect the official policy or position of the United States Air Force, Department of Defense, or the United States Government.

AFIT/GAE/ENY/06-M31

CFD INVESTIGATION OF THE FLOW DYNAMICS INSIDE A SPHERICAL SURFACE INDENTATION

THESIS

Presented to the Faculty

Department of Aeronautics and Astronautics

Graduate School of Engineering and Management

Air Force Institute of Technology

Air University

Air Education and Training Command

In Partial Fulfillment of the Requirements for the
Degree of Master of Science in Aeronautical Engineering

Robert C. Vincent, B.S.M.E.

2d Lt, USAF

March 2006

APPROVED FOR PUBLIC RELEASE; DISTRIBUTION UNLIMITED.

CFD INVESTIGATION OF THE FLOW DYNAMICS INSIDE A SPHERICAL SURFACE INDENTATION

Robert C. Vincent, B.S.M.E.
2d Lt, USAF

Approved:

/signed/

23 Mar 2005

Lt Col R.C Maple, PhD (Chairman)

date

/signed/

23 Mar 2005

Lt Col E. Stephen, PhD (Member)

date

/signed/

23 Mar 2005

Dr. P. King, PhD (Member)

date

Abstract

This study endeavors to identify the flow structure inside and around a dimple surface indentation that passively reduces flow separation, and to generate characterization parameters for the effectiveness of the aforementioned flow structure in boundary layer separation control. In this study, a spherical surface indentation, $\frac{h}{D} = 0.1$, is cut into a flat plate in a diverging channel that creates an adverse pressure gradient. In the baseline flat plate case, the shedding vortices formed by the pressure gradient create an oscillating pressure field throughout the channel. This geometry has been chosen to simulate the adverse pressure gradient present in the flow regime found on a turbine blade experiencing flow separation, while at the same time reducing overall computational cost. The flow regimes to be studied range from Re_D of 2500 to 20500 (by varying the dimple size) and at various boundary layer thicknesses corresponding with a Re_X from 5000 to 95000 (by changing the dimple streamwise location). The points of interest that are verified and closely monitored are the vortical structures inside the dimple, the pressure waves generated by the dimple and the down stream effects. This study ascertains and characterizes the vortical structures that act as the primary mechanism that makes dimples effective in boundary layer separation control and concludes that the flow structures depend on a balance of boundary layer energy and dimple geometry. As dimple size increases the energy trapped in the dimple and its effects (pressure waves, shed vortices, etc...) also increase. As the boundary layer develops and nears separation, the energy in the flow seen by the dimple effectively decreases and the flow structures likewise revert to a lower energy form.

Acknowledgements

First and foremost, I would like to thank my wife for all that she did while I spent the days and nights at AFIT working on this thesis. I would also like to thank LtCol Maple for all of his help and guidance. I owe my father a debt of gratitude for his advice and guidance through the many iterations of this document. Also Dr. Anthenien for spending hours of time that he did not have to derive and re-derive many of the equations that were stone walling the analysis of my findings.

Robert C. Vincent

Table of Contents

	Page
Abstract	iv
Acknowledgements	v
List of Figures	viii
List of Tables	xi
List of Symbols	xii
List of Abbreviations	xiii
 I. Introduction	 1
1.1 Research Goals	1
1.2 Motivation	1
1.2.1 Vortex Generators	3
1.2.2 Dimples and LPT Blades	3
1.2.3 Dimples and Heat Exchangers	5
1.3 Research Approach	6
1.4 Document Structure	6
 II. Background	 7
2.1 Implications For This Investigation	10
 III. Methodology	 12
3.1 Basic Geometry	12
3.2 Flow Parameters	16
3.2.1 Boundary Layer Measurements	17
3.3 Grid	19
3.3.1 Time Integration	21
3.4 Flow Solver	22
3.4.1 Spatial Discretization	22
3.4.2 Time Discretization	24
3.4.3 Boundary Conditions	24
3.5 Visualization	25

	Page
IV. Results	27
4.1 Energy in Flow Structures	28
4.2 Organization and Symmetry of Flow	29
4.3 Size of Recirculation and Wake Zones	32
4.4 Frequency of Pressure Waves	35
4.4.1 Frequency analysis	35
4.4.2 Bulk Shed Phenomena	45
4.5 Downstream Flow effects and Mixing	50
V. Conclusions	56
5.1 Conclusions	56
5.2 Recommendations for future research	57
Appendix A. Case Specific Data	59
Bibliography	62

List of Figures

Figure		Page
1.1.	Inner dimple area	2
1.2.	Tested Pak-B Flow Regimes	4
2.1.	Flow regimes tested by Khalatov	10
2.2.	Comparison of tested flow regimes	11
3.1.	Side view of baseline test channel depicting the shedding vortices resulting from the adverse pressure gradient	14
3.2.	Top view of test channel depicting the streamwise locations of the dimples in the various cases	14
3.3.	Boundary layer seen by the dimple	16
3.4.	Typical undisturbed laminar velocity profile in channel	18
3.5.	Steady trapped vortex on CFD Pak-B turbine blade	19
3.6.	Close up view of grid around dimple	20
3.7.	View of grid from the side	21
3.8.	View of grid from the top with blocks highlighted	21
3.9.	View of grid from the top with blocks highlighted near dimple .	21
3.10.	Boundary condition settings	25
4.1.	Dimple diagram legend	27
4.2.	Energy graduation shown in the dimple flow structures	29
4.3.	Variations of Re_x over constant Re_D	31
4.4.	Inner dimple vortex structure	32
4.5.	Snapshots of the flow structures showing trapped vortices and low-energy recirculation zone flow	34
4.6.	Pressure waves induced by shedding dimple vortices	36
4.7.	Pressure tap data for the baseline channel	37
4.8.	PSD for the pressure data from the baseline channel	37
4.9.	Pressure tap data for $Re_D = 20500$ $Re_x = 5000$	38

Figure		Page
4.10.	PSD for the pressure data from $Re_D = 20500$ $Re_x = 5000$. . .	38
4.11.	Visualization of pressure waves (still frame from animation) $Re_D = 20500$ $Re_x = 5000$	39
4.12.	Pressure tap data for $Re_D = 9500$ $Re_x = 5000$	39
4.13.	PSD for the pressure data from $Re_D = 9500$ $Re_x = 5000$. . .	40
4.14.	Visualization of pressure waves (still frame from animation) $Re_D = 9500$ $Re_x = 5000$	40
4.15.	Pressure tap data for $Re_D = 9500$ $Re_x = 40000$	41
4.16.	PSD for the pressure data from $Re_D = 9500$ $Re_x = 40000$. . .	41
4.17.	Visualization of pressure waves (still frame from animation) $Re_D = 9500$ $Re_x = 40000$	42
4.18.	Pressure tap data for $Re_D = 2500$ $Re_x = 60000$	43
4.19.	PSD for the pressure data from $Re_D = 2500$ $Re_x = 60000$. . .	44
4.20.	Visualization of pressure waves (still frame from animation) $Re_D = 2500$ $Re_x = 60000$	44
4.21.	Snapshots of the flow structures showing unsteadiness and the 'Bulk Flow' feature	46
4.22.	Snapshots of the flow structures showing unsteadiness and the 'Bulk Flow' feature	47
4.23.	Close up of the case $Re_D = 20500$ $Re_x = 77000$	48
4.24.	Snapshots of the flow structures showing the 'Bulk Flow' feature	49
4.25.	Extent of mixing region	51
4.26.	Downstream look at contours of u-velocity for $Re_D = 20500$ $Re_x = 5000$	52
4.27.	Downstream look at contours of u-velocity for $Re_D = 20500$ $Re_x = 66000$	52
4.28.	Downstream look at contours of u-velocity for $Re_D = 9500$ $Re_x = 5000$	52
4.29.	Downstream look at contours of u-velocity for $Re_D = 9500$ $Re_x = 21000$	53

Figure		Page
4.30.	Downstream look at contours of u-velocity for $Re_D = 20500$ $Re_x = 77000$	54
4.31.	Downstream look at contours of u-velocity for $Re_D = 9500$ $Re_x =$ 40000	54
4.32.	Downstream look at contours of u-velocity for $Re_D = 2500$ $Re_x =$ 60000	55

List of Tables

Table		Page
3.1.	Model geometry	15
3.2.	Flow regimes to be tested in this investigation	16
A.1.	Data reduced from $Re_D = 20500$ cases	59
A.2.	Data reduced from $Re_D = 9500$ cases	60
A.3.	Data reduced from $Re_D = 2500$ cases	61

List of Symbols

Symbol		Page
Re_c	Chord based Reynolds number	4
Re	Reynolds number	7
C_d	Drag Coefficient	7
Re_D	Diameter based Reynolds number(= $\frac{\rho \vec{v} D}{\mu}$)	8
D	Dimple diameter	11
h	Depth of dimple indentation	12
D	Dimple diameter	12
X_{LE}	Leading edge of dimple x-wise location	13
U_∞	Free-stream velocity	16
\dot{E}_δ	Boundary layer energy	17
δ_{LE}	Leading edge boundary layer thickness	17
θ	Momentum thickness	17
δ^*	Displacement thickness	17
H	Shape factor	18
Δt	Physical time step	21
ρ	Density	22
∇P	Pressure gradient	22
\vec{g}	Gravity vector	22
\vec{F}	Body force vector	22
\vec{v}	Velocity vector = $u\hat{i} + v\hat{j} + w\hat{k}$	22
$\bar{\tau}$	Stress Tensor	22
I	Identity matrix	22
μ	Viscosity	22
St	Strouhal number	59

List of Abbreviations

Abbreviation		Page
UAV	Unmanned Aerial Vehicles	1
LPT	Low Pressure Turbine	1
AFIT	Air Force Institute of Technology	8
CFD	Computational Fluid Dynamics	22
SIMPLE	Semi-Implicit Method for Pressure-Linked Equations . . .	23
MUSCL	Monotone Upstream-Centered Schemes for Conservation Laws	23
PSD	Power spectrum density	35

CFD INVESTIGATION OF THE FLOW DYNAMICS INSIDE A SPHERICAL SURFACE INDENTATION

I. Introduction

In the high-altitude, low-speed loiter missions typical of Unmanned Aerial Vehicles, (UAV), the suction sides of low pressure turbine (LPT) blades suffer from large separation losses while operating at the low Reynolds numbers (Re) typical of that mission profile. This separation zone can span from 20% to 40% of the overall chord length, which reduces the blade efficiency and leads to significant turbine power losses. In order to improve the turbine efficiency, both active and passive flow control techniques are employed; among the potential passive techniques, shallow dimples ($h/D=0.1$) are considered very promising. They provide reduced pressure losses at $Re_C < 40,000$ and, when compared with other passive techniques, the spherical dimples have demonstrated the best results with respect to reduction in separation losses without added drag penalties at higher Re_C [2, 15, 20].

1.1 *Research Goals*

This research strives to increase the understanding of the flow dynamics, the internal flow structures and the parameters that characterize them in and around a single spherical dimple within an infinite array of dimples. In Fig. 1.1, the red area highlights the area of focus for this research. Furthermore, this study is designed to be useful for flows where an adverse pressure gradient is present such as turbine blade modelling.

1.2 *Motivation*

The effect of boundary layer separation control can be achieved through a number of methods both active and passive. Among the active techniques are wall jets,

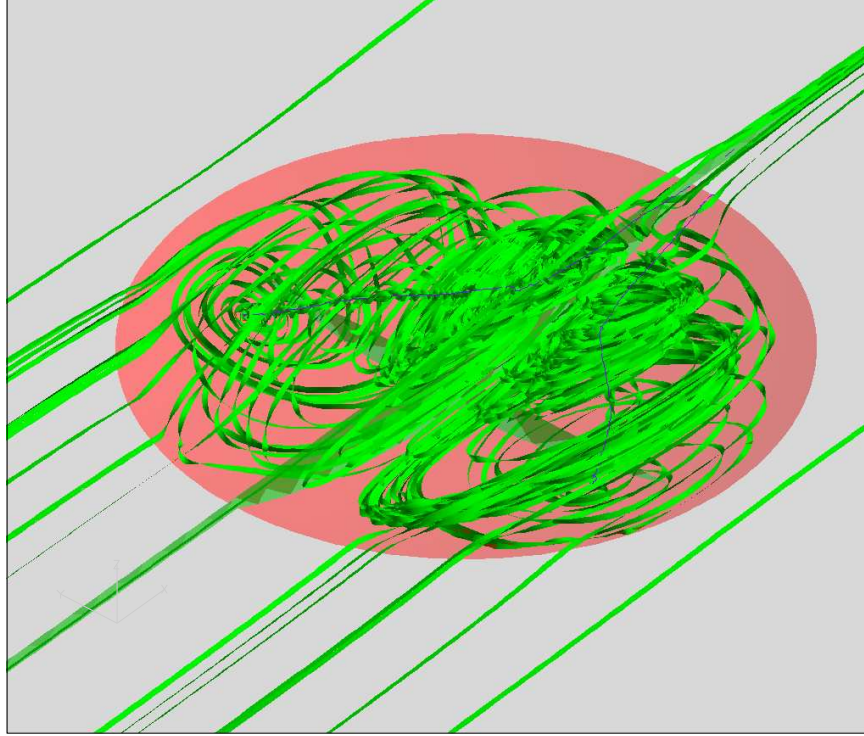


Figure 1.1: Inner dimple area.

plasma generation strips, and boundary layer suction. Wall jets inject high energy flow into the boundary layer helping it to stay attached. Plasma generation strips use an electric arc to energize and turn the flow into the wall keeping it attached. Boundary layer suction removes the low energy flow in the boundary layer allowing the high velocity flow to remain attached. All of these active techniques are very difficult and expensive to manufacture and each adds subsystems to a jet engine that must be maintained. The cost of these techniques is prohibitive and continues to motivate the pursuit of better passive techniques.

Most of the passive techniques for boundary layer control involve the generation of a streamwise vortex. This flow structure can be very stable and can extend relatively long distances. Streamwise vortices can serve to break up the spanwise rolling vortex produced by the boundary layer that eventually facilitates flow separation. The physical structure that produces a streamwise vortex is known as a vortex generator.

1.2.1 Vortex Generators. Vortex generators are generally classified into two categories, protruding and recessed. Their function is to create a vortex that will mix high-energy free-stream fluid particles with low energy boundary-layer fluid particles. This effect has numerous applications from boundary layer separation control to increasing the thermal conductivity of flows — allowing for higher performance airfoil geometries and smaller heat exchangers.

1.2.1.1 Protruding Vortex Generators. The main benefit of a protruding vortex generator over a recessed one is that the effects on the flow generally travel farther down stream. Though they are more effective at mixing the flow field, the added drag penalty resulting from the surface extending into the flow can often offset the efficiency gained by keeping the flow attached. Furthermore, this drag penalty grows with velocity; in the case of a turbine blade, the improvements at low Re would be greatly overshadowed by the losses at higher Re , thus making a protruding device unreasonable [14].

1.2.1.2 Recessed Vortex Generators. Various forms of recessed vortex generators exist, including simple grooves of various profiles, dimples, and porous cavities designed to take advantage of adverse pressure gradients and create circulation around separation points. A unique quality of dimples is that their effects can be focused to a target Re_D . They are relatively innocuous at off-design conditions [2, 14, 20]. In some cases dimples in flat plates have been shown to reduce the drag coefficient when compared with a smooth surface [8]. Considering the effect they have on the flow, creating complex vortex structures and mixing the flow so thoroughly, the fact that they reduce the overall drag is remarkable. This suggests that the performance of the airfoil section or turbine blade could be improved at both low and high Re .

1.2.2 Dimples and LPT Blades. Lake [14] conducted experimental research into the use of passive techniques to regulate the boundary layer separation problem found on LPT blades. He established a baseline understanding of the separation flow

regime and the Re_c when the separation takes place testing the popular Pak-B airfoil in a linear cascade tunnel. He then set out to compare the results of using a V-groove, a trip wire, and dimples to reattach the flow. He found that the dimples kept the flow attached with a lower penalty at higher Re_c than the other methods. To produce the dimples he used a 2-inch ball-end mill to make a series of depressions into the blade surface at various chord locations. The result of the hemispherical shape of the mill and the curvature of the airfoil made his dimples elliptical, with the major axis in the cross-flow orientation. The results of this research were encouraging and suggested that dimples in the proper configurations could in fact solve the separating flow issue without adversely affecting the performance at higher Re_c .

Rouser [20] extended Lake's research and ran experiments on the Pak-B blade down to a Re_c of 25,000. Rouser also introduced tests of asymmetric, $\frac{1}{2}$ -ellipse, dimples. Rouser found that the dimples farthest downstream (at 65% c) had the most advantageous effect on the flow. He developed a CFD model to better visualize what the experimental model was doing. The CFD model did not, however, successfully duplicate the experimental results .

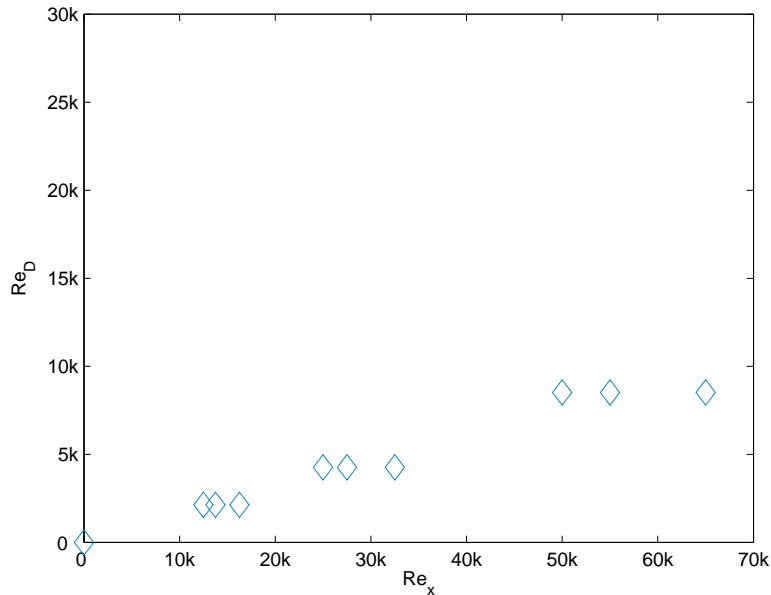


Figure 1.2: Tested Pak-B Flow Regimes.

Following Rouser, Casey [2] took the Pak-B blade and added a second row of dimples at 75% c and tested various lateral spacings trying to characterize the flow properties. The results of Casey’s experimental work were ambiguous as to which configuration was ‘best.’ His computational models did, however, sufficiently capture the flow effects. This indicated that future studies, to identify trends and further characterize the flow structures and their downstream effects, could be accomplished in the computational realm. The extent of Casey’s computational research was limited by extremely long computation times, the unwieldy size of the data sets and the limited resources to process them. An approximation of the flow regimes covered by the research on the Pak-B blades can be seen in Fig. 1.2.

1.2.3 Dimples and Heat Exchangers. The flow phenomena created by dimples which help energize boundary layers and keep them attached to the suction surface of the Pak-B blades is the same mechanism that the heat transfer community is interested in to better mix the thermal boundary layer with the free-stream flow to enhance heat transfer from a surface. Many researchers have investigated the heat transfer properties and potential of dimples, desiring to reduce the size of heat exchangers and the fixtures that they require. The research in this area has dealt primarily with flat-plate configurations of dimple arrays. In the 70’s and 80’s Soviet researchers began an exhaustive literature base of dimple flow structures with turbulent freestream conditions. Isaev [7,8], Terekov [24] and Kiknadze [13] took up the study and have continued to develop the understanding of turbulent flows over dimpled surfaces. Unfortunately, relatively little effort has been dedicated to laminar cases. Isaev [8] studied the vortex structures of various dimple configurations under laminar conditions, but were largely in the same very low energy, $Re_D \leq 1500$ flow regime. Ligrani [17] investigated the flow structures in an array of dimples in a channel but again his flow regime was turbulent. In general, a detailed characterization of the complex vortical structures that form within a single dimple in laminar flow and

how these structures change with respect to leading edge flow conditions and dimple size/depth is still lacking.

1.3 Research Approach

This investigation utilized a commercial CFD code, FLUENT[®], to solve the flow over a flat plate with a dimple indentation. The pressure waves induced by shedding vortex structures are a unique element of the environment around a turbine blade experiencing separated flow. In order to simulate a similar environment, the channel includes an adverse pressure gradient. Due to the fact that this study aims to characterize trends in the dimple flow patterns, no effort was made to match shed vortex frequencies, shed vortex magnitudes, or surface static pressure gradients with those experienced on the Pak-B turbine blades. Fundamentally, this experiment uses a flat plate in an adverse pressure gradient generated by the diverging inviscid wall defined by Eq. 3.1 to roughly model the turbine blade suction surface environment. The grids model an infinite row of dimples of various sizes and at various streamwise locations. Visualization and data reduction are accomplished through a combination of FIELDVIEW[®], MatLab[®] and FLUENT[®]'s built in data export and visualization tools.

1.4 Document Structure

Chapter One presents a background of relevant experimentation and sets up the motivation for this research effort, explaining the key terminologies, ideas and concepts. Chapter Two provides a historical summary of results of prior experiments and outlines the structure of this research effort. Chapter Three is dedicated to the methodology of this investigation, details of the flow solver, the computational model and the visualization techniques. Chapter Four provides results and analysis of the individual flow solutions computed in this study, and Chapter Five presents conclusions and suggestions for future research.

II. Background

One of the earliest investigations of the flow features near surfaces with spherical dimples was made by Bearman and Harvey [1]. This study assessed the effects of dimples on the flow around a cylinder as it underwent transition from subcritical to post-critical flow. The results of this study demonstrated the effectiveness of dimples as a technique for causing early boundary layer transition without the drag penalties associated with surface roughness (sand). Their research revealed that unlike a smooth or roughed round ball, the drag curve of a dimpled ball remains almost constant at the post-critical Re . This data spawned the conclusion that dimples reduce pressure drag by triggering laminar-turbulent transition without the added drag penalties of surface roughness. Experiments carried out on a dimpled circular cylinder showed that shallow dimples ($\frac{h}{D} = 0.1$) cause transition at a lower Re than that for a smooth cylinder [1].

Dimples affect the flow around a circular cylinder in a similar manner to the flow around a golf ball. At low Re the Strouhal numbers correspond to that for a smooth cylinder, while at high Re it approaches a value above 0.25. In between, the Strouhal number reaches a maximum ($St=0.32$) at about the same Re that corresponds with the minimum value of the drag coefficient, C_d . As recorded, the variation of Strouhal number with Re for the dimpled cylinder mirrors the variation of C_d with Re [1]. This suggests that the reduction in drag is related to the vortex shedding frequency. The shedding vortices are thought to be the feature generated by dimples that help flow control.

Single dimples on a flat plate and multiple-dimpled flat plates are the most studied configurations. Flow over a multiple-dimpled flat plate (8-20 rows) related to heat exchanger design are well documented in many publications. In the end, it should be noted that the bulk of available publications cover primarily turbulent flow (except the data of Lake [14], Rouser [20], Casey [2], Khalatov [9] and Isaev [8]), but actually little research has dealt with laminar flow over and inside of dimples.

Complex vortex structures inside a cylindrical hole on a flat plate are described in the early experiments of Wighardt [25]. The peaks in the function representing the minimum increase in drag, $\Delta C_{D_{min}} = f\left(\frac{h}{D}\right)$, correlate with changes in the flow structures; the minimum increase was found at $0.1 \leq \frac{h}{D} \leq 0.2$ and $\frac{h}{\delta_o} = 0.6$. Based on these experiments, Lavrent'ev and Shabat [16] predicted that the generation of unstable ring vortices over a round dimple are the mechanisms that reduce the drag penalties. Gromov [4] and Ligrani [17] further investigated the inner dimple flow structure in their flow visualization experiments. They concluded that tightening spirals, helical streamlines and horseshoe (twin) vortices exist inside a dimple and lead to its downstream flow effects. Khalatov [12] made the observations of the growing complexity of the internal vortical structure with rise in Re_D .

A review of the available literature revealed that little has been done to characterize the flow effects of various shapes of dimples. Bearman and Harvey [1] arrived at the conclusion that the hexagonal shaped dimples suited the golf ball problem best due to the added flow characteristics of the edges. The heat transfer community has developed data on cylindrical dimples — dimples with sharp edges and flat bottom surfaces — and has found that in some cases they have more advantageous flow effects than the spherical counterparts. Data reported in Terekhov [23] has shown that a side-to-side flow mechanism can also be found inside cylindrical dimples. Hiwada [5] published that both single spherical and single cylindrical dimples have demonstrated the heat transfer minimum at $h/D=0.2$. The recent investigation of Moon & Lau [18] shows that cylindrical dimples on a flat plate produce higher overall heat transfer, based on the projected area and lower pressure drop, than spherical dimples with the same diameter and depth.

Lake's elliptical dimples occurred by accident (a two inch ball mill sunk into a curved surface to arrive at an ellipse), and the round bottoms were merely based on Bearman. The half ellipse dimples of Rouser were only compared with the full ellipse dimples and were found to be less effective. Elliptical dimples — previously researched at AFIT (Lake [14], Rouser [20], Casey [2]) — show great promise. Isaev [8] has also

extended some of his experiments into the realm of asymmetry with combinations of curvatures and depths, unfortunately his tests were all done at extremely low Reynolds numbers ($100 \leq Re \leq 2500$) and found only the expected stable pinned horseshoe vortex.

According to the literature [9, 11], the flow structure within and downstream of a single dimple can depend on the dimple geometry (spherical, cylindrical, asymmetrical), dimple depth (h/D), dimple based Reynolds number — Re_D , pre-dimple boundary layer thickness to dimple depth ratio $\frac{h}{\delta_{99}}$ and the shape of the dimple edge (sharp, or rounded-off).

It is interesting to note that the findings of Casey agree with the flat plate investigations of Khalatov where in the lower range of Re_D a single, stable, trapped horseshoe vortex was found inside the dimple. This discovery lends question to the aforementioned sources' historical hypotheses that the dimples trigger an early transition to a turbulent boundary layer and the beneficial effects are a result of transition. However, if the effect can be modelled with a laminar code, the effect could be the result of a mechanism other than transition.

Khalatov et al. [11] attempt to ascertain the peak effective (based on downstream velocity profiles, shape factor and Strouhal number) Re_D for a given boundary layer thickness to dimple depth ratio. Their effort used measurements of the boundary layer profile aft of the dimple to determine the effect of the dimple on the flow, as well as flow visualization through dye injection to try and ascertain the mechanisms present in the flow.

Khalatov et al. [10, 12] recently published a number of papers that attempt to give a baseline understanding to this overall question of the characterization of the dimple flow. His tests were run without isolating Re_x from Re_D , and thereby fail to provide more than a few valid data points as seen in Fig. 2.1, from which flows could be characterized.

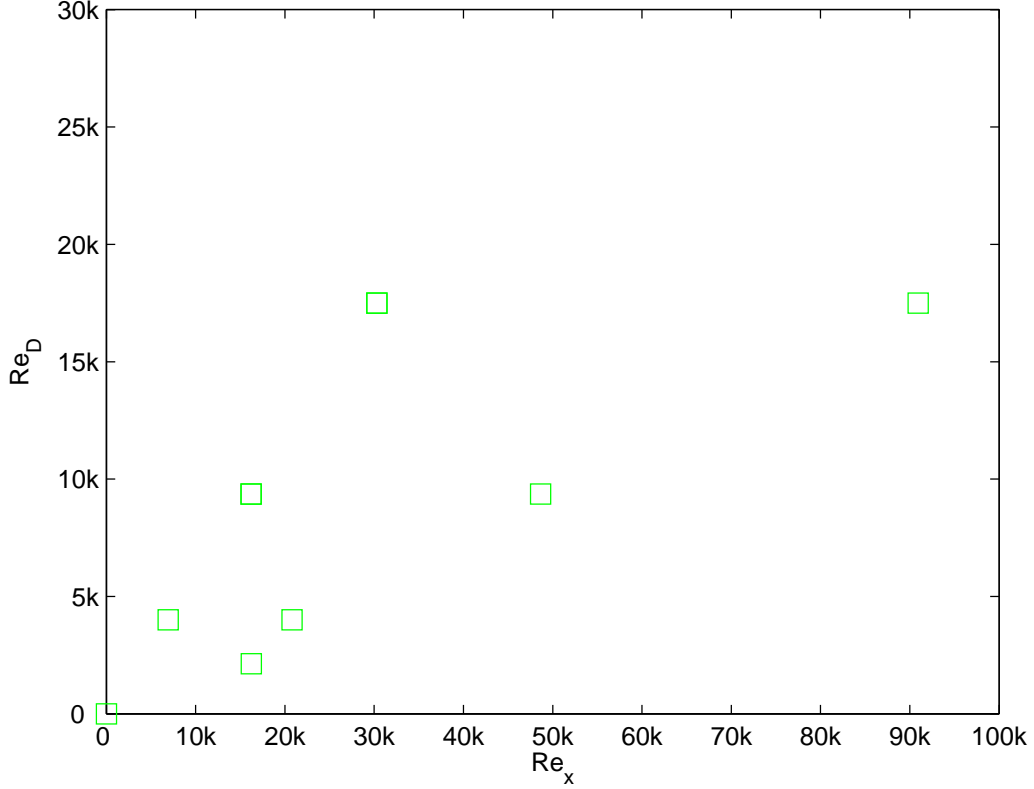


Figure 2.1: Flow regimes tested by Khalatov.

2.1 Implications For This Investigation

The optimal setting that was found in Khalatov's research [11] was a $Re_D \approx 9500$. $Re_D \approx 9500$ is a good mid point in the flow regimes of interest and due to the encouraging results of Khalatov, it sets the size for one of this investigations dimples. This study aims to reduce the number of characterization parameters to as few as possible and still maintain accurate characterizations of the gross structures within the flow. For this investigation the parameter $\frac{h}{D}$ remains constant and $= 0.1$. Figure 2.2 roughly depicts the flow regimes of the previously mentioned research efforts and their relative positioning to one-another. This is an approximated comparison, as the reduction of the turbine blade data from Re_c to Re_x is not rigorous and does not fully describe the boundary layer properties at the dimple. In reality, the Re_x that would produce an equivalent boundary layer profile to those seen on the Pak-B

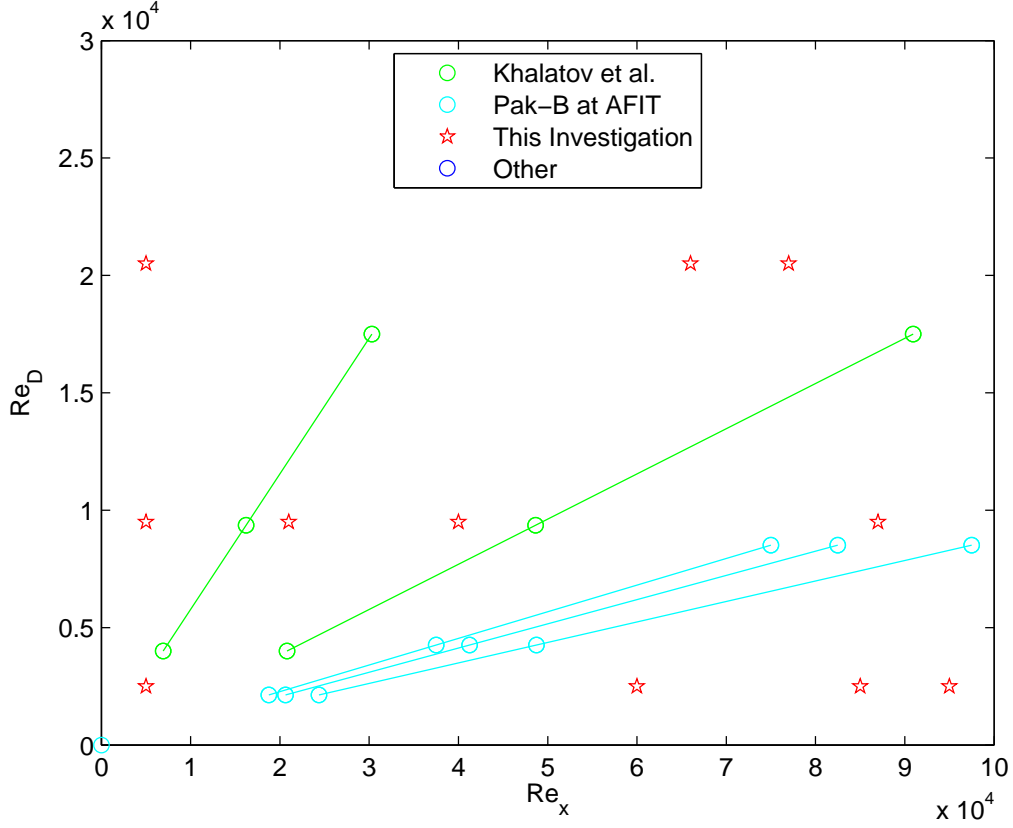


Figure 2.2: Comparison of tested flow regimes.

blades would be larger and thereby shift the flow regime points further to the right. The comparison is useful, however, to qualitatively relate the different studies and determine where the gaps are in the big picture of understanding what is happening in laminar flows over dimpled surfaces. The cases chosen to study in this investigation aim to characterize the dimple flow at all of the flow regimes within Fig. 2.2.

Figure 2.2 also shows the weakness in developing models and running them at different velocities to alter the Re_D parameter. This practice produces lines on the above plot whose slope is the ratio between streamwise location and dimple diameter D . Re_D alone is insufficient as a defining parameter for a dimple. This investigation will isolate Re_x from Re_D in an effort to identify which flow structures are a result of the boundary layer and which ones are a result of the dimple size.

III. Methodology

The overall computational model is comprised of, the physical/grid models, the flow solver and the visualization techniques. Without adequate understanding of the processes involved, any one of these three items could render meaningless answers.

3.1 Basic Geometry

To accomplish the goals of this investigation, a simplified model geometry that reduces computational cost and maintains applicability to the turbine environment is needed. This investigation models an infinite row of spherical dimples on a flat plate in a diverging channel.

The first simplification made is that the top wall of the channel is inviscid. This greatly reduces the grid resolution requirements by not needing to capture a boundary layer. This simplification does not affect the flow solution since the only parameter generated by the top wall that is needed for the solution is pressure and pressure information can propagate through a very coarse mesh without distortion.

Bearman and Harvey [1] found that the effectiveness of the dimples was greatest between a $\frac{h}{D} = [0.1, 0.2]$. To reduce the number of models, this investigation only considered one ratio, $\frac{h}{D} = 0.1$.

Another major simplification is modelling a flat plate instead of a full turbine blade. According to Syred et al. [22] there is no significant difference in the flow dynamics in and around a dimple located on a flat surface versus one on a convex surface such as the suction side of a turbine blade. Their experiments demonstrated a net change of less than 4% in the critical parameters for the dimples in a convex surface versus dimples of identical geometry in flat surfaces. They also concluded that the pressure gradient over the dimpled surface was the primary cause for the larger differences present between the dimple in the concave surface versus the dimple in the flat plate.

In order to further reduce the computational runtimes and the data storage requirements, application of this finding is made to this experimental setup. This simplification reduces the grid and data storage requirements by almost 50%, and shortens the computation time from six weeks (Casey [2]) to just over two weeks. Furthermore, it allows for the qualitative comparison of data between the previous turbine experiments and that of the heat transfer community on flat plate and channel flows.

This investigation, as mentioned previously in Section 1.3, has a built in adverse pressure gradient which induces shedding vortices on the flat plate. A series of baseline grids (without dimples) were made to determine an appropriate geometry for the diverging, inviscid, top-wall. The final geometry for the diverging wall was chosen because it forced shedding at an ideal point, about half way through the channel, but did not pull the shedding vortices too far from the viscous wall as seen in Fig. 3.1. The final diverging wall is approximated by Eq. 3.1. The resulting pressure gradient is curve fit to Eq. 3.2.

$$Z(x) = \left\{ \begin{array}{ll} \{-0.06 \leq x \leq 0.2\} &= \begin{array}{l} 0.04995 + 0.0160601 * x + \\ 0.376516 * x^2 + 0.371514 * x^3 \end{array} \\ 0.2 < x \leq 0.34 &= 0.15 \end{array} \right\} \quad (3.1)$$

$$P(x) = -4.31586 + 19.6724 * x + 866.162 * x^2 - 1039.76 * x^3 - 2381.14 * x^4 \quad (3.2)$$

The depth of the test channel = $3 * D$ so that in the infinite row of dimples, a space = $2 * D$ exists between dimple edges. The rest of the critical parameters that are specific to each test case can be found in Table 3.1. Figure 3.2 gives a more visual depiction of the leading edge of dimples x-wise locations, X_{LE} , and the Re_x values that are calculated using them. Following the divergent portion of the channel is another parallel portion to allow the flow time to reattach/redevelop such that the FLUENT® ‘outflow’ boundary condition would be appropriately applied.

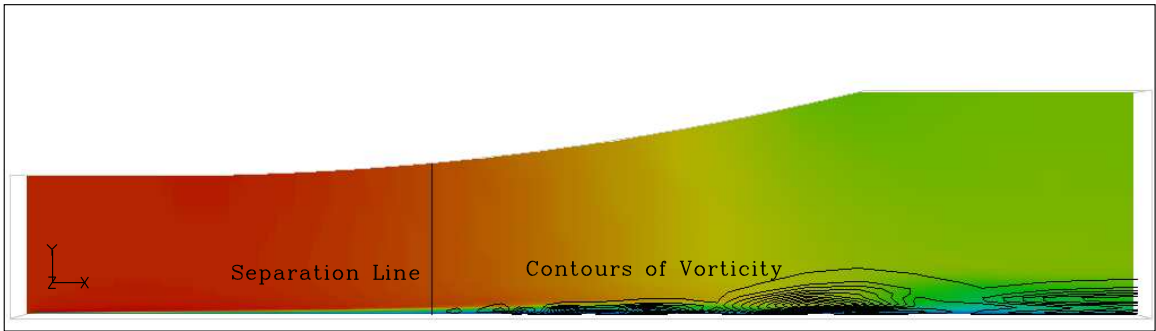


Figure 3.1: Side view of baseline test channel depicting the shedding vortices resulting from the adverse pressure gradient. Colored by u velocity with contours of spanwise vorticity.

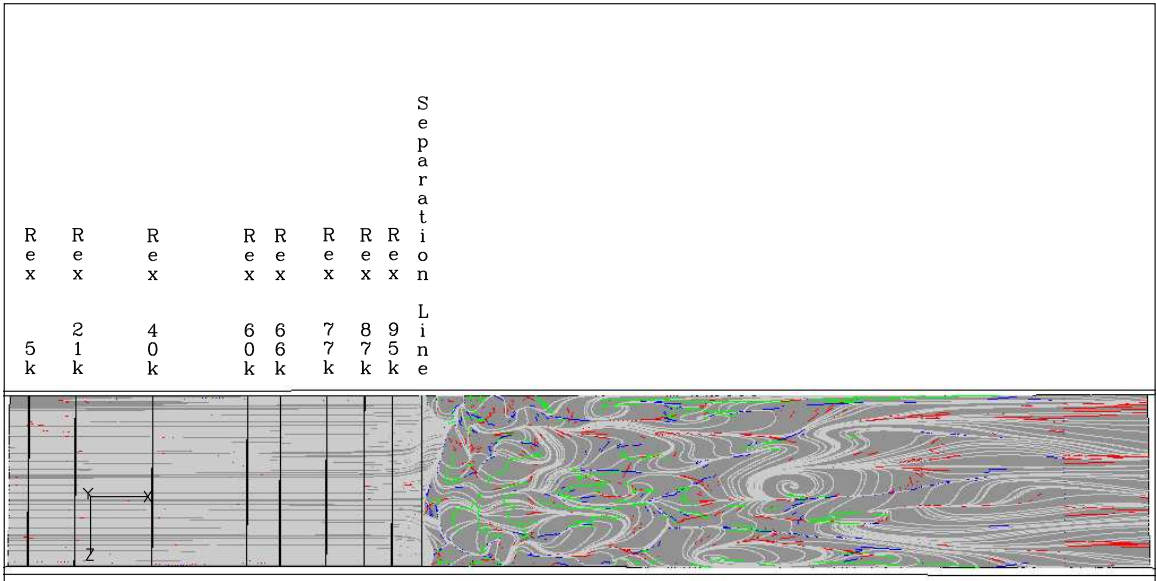


Figure 3.2: Top view of test channel depicting the streamwise locations of the dimples in the various cases.

Table 3.1: Model geometry.

Re_D	D (m)	Re_x	x_{LE} (m)	h (dimple depth (m))	Spherical radius
20500	0.03	5000	0.0058	0.003	0.039
	0.03	66000	0.096051	0.003	0.039
	0.03	77000	0.112365	0.003	0.039
12000	0.01756	13000	0.01976	0.001756	0.022774
9500	0.013	5000	0.0052	0.0013	0.0182
	0.013	21000	0.02356	0.0013	0.0182
	0.013	40000	0.050905	0.0013	0.0182
	0.013	87000	0.120574	0.0013	0.0182
2500	0.003651	5000	0.007756	0.000365	0.004748
	0.003651	60000	0.084409	0.000365	0.004748
	0.003651	95000	0.01325524	0.000365	0.004748

3.2 Flow Parameters

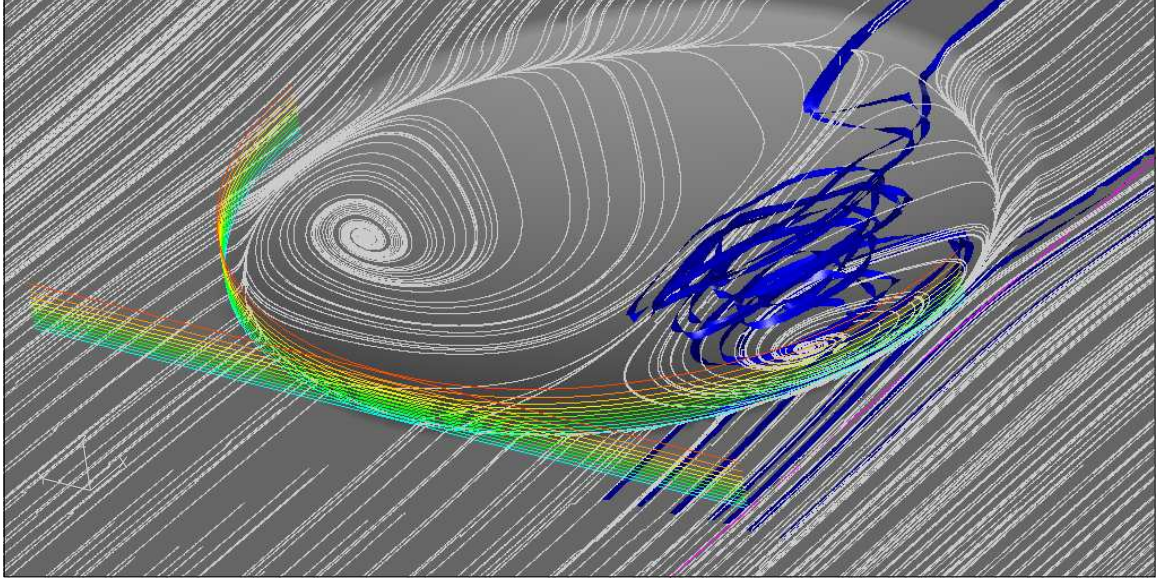


Figure 3.3: Boundary layer seen by the dimple.

This investigation utilized a constant free-stream velocity, $U_\infty = 10 \frac{m}{s}$, and varied the dimple size and downstream locations to manipulate the Re_D and Re_x parameters, outlined in Table 3.2. When deciding the flow parameters to use in characterizing the

Table 3.2: Flow regimes to be tested in this investigation.

Cases to be tested					
$Re_D = 20500$	5k		66k		77k
$Re_D = 12000$		13k			
$Re_D = 9500$	5k	21k	40k		87k
$Re_D = 2500$	5k			60k	95k
	Re_x				

dimples, it is important to remember that the dimples do not really feel the effect of the freestream flow. They instead react to the conditions of the flow in the boundary layer. The best way to quantify the pre-dimple flow in terms relevant to the dimple

and its internal flow structure, would be to quantify boundary layer energy, given by Eq. 3.3, momentum thickness, and spanwise projected area relative to the dimple, approximated as $\delta_{99} * D$ as seen in Fig. 3.3.

$$\dot{E}_\delta = \frac{1}{2} u^3 \delta_{LE} D \quad (3.3)$$

where:

\dot{E}_δ	Boundary layer energy
u	Streamwise velocity
δ_{LE}	Leading edge boundary layer thickness
D	Dimple diameter

When calculating the projected spanwise area, it is important to note that the boundary layer seen by the dimple is actually longer than simply the projected spanwise area of the dimple or in this case the diameter because upstream flow can be drawn into the dimple as shown in Fig. 3.3. It is more accurately represented by looking at oil flow or streak lines and finding the extent of streamline cross-flow deformation and calculating the boundary layer length between the last streak lines that enter the dimple cavity (magenta line on Fig. 3.3).

3.2.1 Boundary Layer Measurements. Ideally, quantification of boundary layer energy would be elementary and the application of Eq. 3.3 quite simple. However, due to the added complexity in the geometry of this problem the seemingly simple application of boundary layer theory is rendered inappropriate. The problem rests with the combination of the adverse pressure gradient and the inviscid wall. Together they produce a velocity profile similar to a wall jet, depicted in Fig. 3.4. The standard measures used to characterize a boundary layer are: streamwise velocity profiles, momentum thickness, θ , (Eq. 3.4) and displacement thickness, δ^* , (Eq. 3.5)

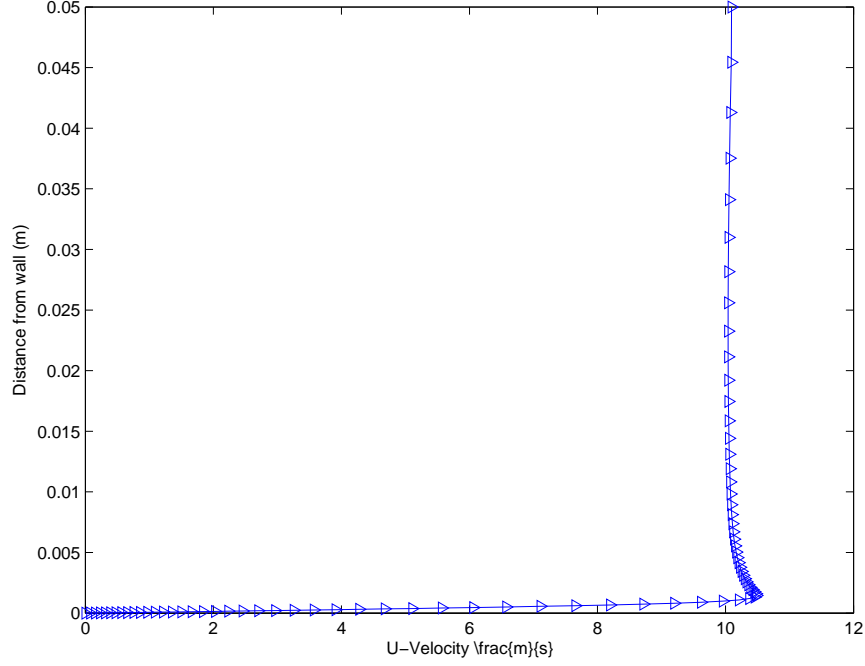


Figure 3.4: Typical undisturbed laminar velocity profile in channel.

and shape factor, H , (Eq. 3.6).

$$\theta = \int_0^{\infty} \frac{u}{U_{\infty}} \left(1 - \frac{u}{U_{\infty}}\right) dy = \frac{\delta^*}{H} \quad (3.4)$$

$$\delta^* = \int_0^{\infty} \left(1 - \frac{u}{U_{\infty}}\right) dy = \delta_{99} - \frac{1}{U_{\infty}} \int_0^{\delta_{99}} u dy \quad (3.5)$$

$$H = \int_0^{\infty} \left(\frac{u}{U_{\infty}}\right) dy = \frac{u}{U_{\infty}} \int_0^{\delta_{99}} u dy \quad (3.6)$$

Due to the limitations of the set up of this experiment these quantities cannot be calculated. The top-inviscid wall causes a compression in the streamlines that forces $\delta^* = 0$ at the top wall. The acceleration in U just over the boundary layer results in a negative value of θ . The flow in this region is technically gaining momentum, so the calculated deficit is negative. There is a deficit found nearer to the inviscid wall, but the deficit caused by the adverse pressure gradient tends to obscure the

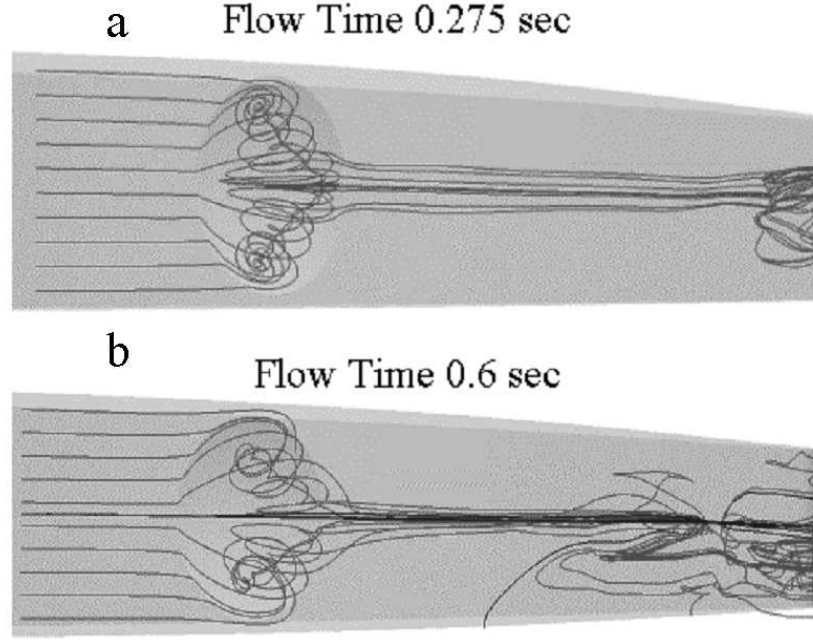


Figure 3.5: Steady trapped vortex on CFD Pak-B turbine blade [2].

relatively small contribution from the viscous forces interacting with the bottom wall. This issue remains unresolved for this investigation, but a solution is not necessary for a qualitative characterization of the flow dynamics within the dimple itself. An approximate quantification of the boundary layer parameters is built into the Re_x figure used in this investigation.

3.3 Grid

In Casey's thesis [2] it was discovered that a purely laminar CFD model could capture the effect of the dimple on the turbine blade, as seen in the flow depicted in Figure 3.5. Based on that finding, this investigation does not utilize a turbulence model. Using Eq. 3.7 as a guideline for calculating the grid spacing off a wall in laminar flow [3], the first cell must be spaced no more than $1.05E^{-4}m$.

$$y_p \sqrt{\frac{U_\infty}{\nu x}} \leq 1.0 \quad (3.7)$$

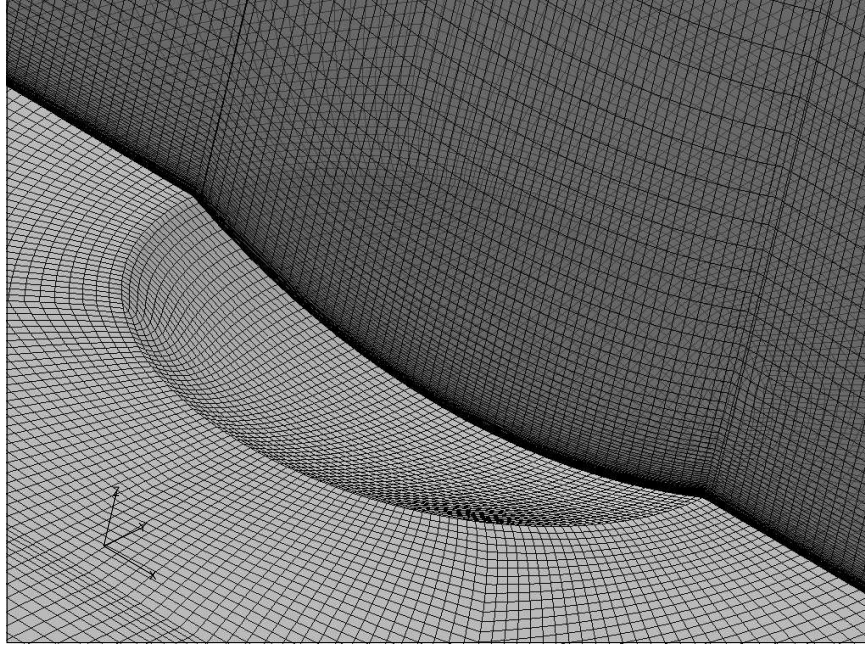


Figure 3.6: Close up view of grid around dimple.

Due to the desire to get more cells inside the dimple, tighter spacing was used for this research. The spacing off the wall begins at $\Delta z_1 = 5E^{-6}m$ and grows using a hyperbolic tangent function with the final node resting at $\Delta z_{50} = 0.0045m$ from the inviscid wall. This should be more than sufficient for accurate boundary layer capture. The dimple had 240 nodes on its perimeter, 3400 nodes(horizontally)on its interior and about 35 in its depth. All together about 121k cells are located inside the dimple, shown in Fig. 3.6. The overall streamwise spacing is stretched and compressed to maximize the resolution of the grid $2 * D$ upstream of the dimple and $3 * D$ down stream of the dimple. The spacing remains sufficient to capture qualitative features and trends up to the separation line, but beyond that the spacing is too coarse to extract reliable data. The overall streamwise distribution of the cells can be seen in Fig. 3.7. The overall horizontal distribution of the cells is depicted in Fig. 3.8. The complete model consists of ≈ 1.7 million cells in 18 blocks shown as different colors in Fig. 3.8 and Fig. 3.9.

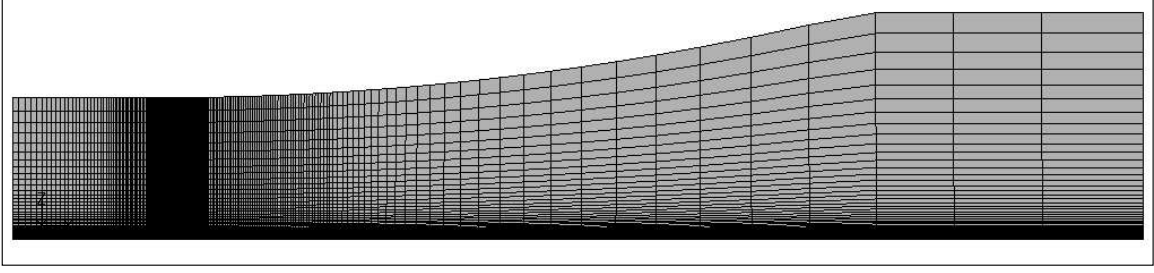


Figure 3.7: View of grid from the side.

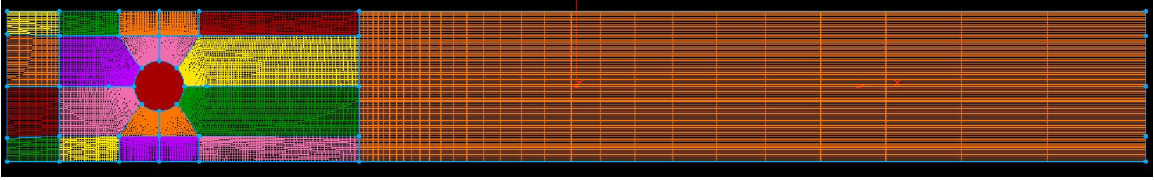


Figure 3.8: View of grid from the top with blocks highlighted.

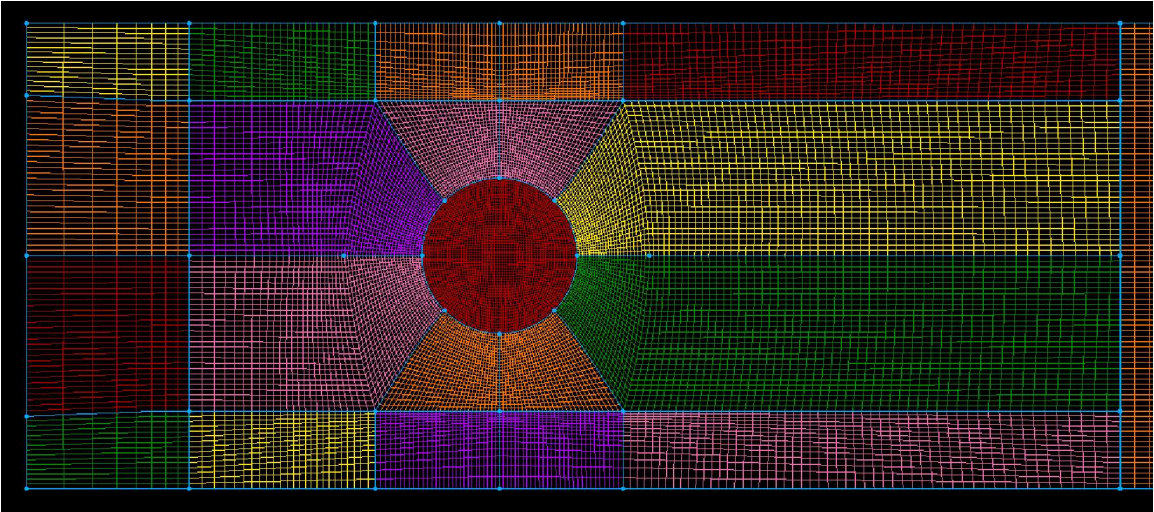


Figure 3.9: View of grid from the top with blocks highlighted near dimple.

3.3.1 Time Integration. A convergence study which tested time steps (Δt) from $1.0E^{-6}$ to $1.0E^{-3}$ with one of the large dimple models showed that a time step size $= 1.0E^{-4}s$ would yield similar flow structures as the smaller step sizes. Based on this result all simulations were run using a time step of $1.0E^{-4}s$. The minimum physical time given for flow development was 2.5 seconds after which data was drawn for analysis and animations.

3.4 Flow Solver

This investigation utilizes the FLUENT[®] CFD solver. Due to the fact that these cases run at a physical velocity of $10\frac{m}{s}$ -which corresponds to a sea level Mach number of 0.03, for this research, FLUENT[®] is set up to solve a discretized form of the Navier Stokes Equations — Eq. 3.8 with a segregated solver, solving momentum and pressure separate from one another [3].

$$\frac{\partial}{\partial t} (\rho \vec{v}) + \nabla \cdot (\rho \vec{v} \vec{v}) = -\nabla P + \nabla \cdot (\bar{\bar{\tau}}) + \rho \vec{g} + \vec{F} \quad (3.8)$$

where:

- ρ Density
- ∇P Pressure gradient
- \vec{g} Gravity vector
- \vec{F} Body forces
- \vec{v} Velocity vector = $u\hat{i} + v\hat{j} + w\hat{k}$
- $\bar{\bar{\tau}}$ Stress Tensor = $\mu [(\nabla \vec{v} + \nabla \vec{v}^T) - \frac{2}{3} \nabla \cdot \vec{v} I]$
- I Identity matrix
- μ Viscosity

When density is constant, the continuity equation must be altered to solve for pressure directly. For cases where the flow is known to be incompressible, FLUENT[®] gives the option to run a SIMPLE scheme [3].

3.4.1 Spatial Discretization. FLUENT[®] presents a number of options for the spatial discretization schemes. Here the schemes chosen for this investigation will be described. For the segregated solver, FLUENT[®] breaks the overall process of discretization of the Navier Stokes equations into four parts, pressure-velocity coupling, pressure, density, and momentum [3].

3.4.1.1 SIMPLE Scheme Option. The SIMPLE (Semi-Implicit Method for Pressure-Linked Equations) scheme uses a relationship between velocity and pressure corrections to enforce mass conservation and close the equations to solve the pressure field [3]. This scheme guesses a value for P — the pressure field — and solves the face fluxes, then iterates to a converged solution [3].

3.4.1.2 2nd Order Pressure Scheme. FLUENT[®] stores pressure and velocity at cell centers in part of a co-located scheme [3].

$$a_P u = \sum_{nb} a_{nb} u_{nb} + \sum p_f A \cdot \hat{i} + S \quad (3.9)$$

The discretized x-momentum equation, Eq. 3.9, requires the value of the pressure at the faces between cells. A second-order interpolation scheme [3] is used to compute the face pressures from the cell center values. This scheme provides some improvement over the first-order standard and linear schemes available in FLUENT[®] and is well suited for this case. The drawbacks of the second-order scheme are not applicable for this flow since they predominately affect flows with discontinuous pressure gradients or mixtures [3].

3.4.1.3 Density. As stated earlier, the flow solved in this investigation is incompressible so density is nearly constant. In these cases FLUENT[®] utilizes a simple arithmetic averaging for the density extrapolations [3].

3.4.1.4 MUSCL Scheme. In the models simulated in this research, a third order MUSCL scheme, Equations 3.10 – 3.12, is employed to accomplish the necessary spatial extrapolation of cell-centered values to the cell faces [3].

$$\phi_f = \theta \bar{\phi}_f + (1 - \theta) \phi_{f,SOU} \quad (3.10)$$

$$\phi_{f,SOU} = \phi + \nabla \phi \cdot \Delta \vec{s} \quad (3.11)$$

$$\nabla\phi = \frac{1}{V} \sum_f^{N_{faces}} \tilde{\phi}_f \vec{A} \quad (3.12)$$

where:

ϕ_f	Face value of arbitrary property ϕ
$\bar{\phi}_f$	Value of ϕ_f interpolated at the face center
$\phi_{f,SOU}$	ϕ_f computed using the second-order upwind scheme as described in Equations 3.11 and 3.12
V	Cell volume
\vec{A}	Cell face area vector

This third-order convection scheme is developed from the original MUSCL (Monotone Upstream-Centered Schemes for Conservation Laws) by crossing a central-difference scheme and second-order upwind scheme [3]. The MUSCL scheme helps prevent numerical diffusion and significantly improves solutions with complex 3-dimensional flows. FLUENT[®] uses this scheme without a limiter which would pose problems for a case where discontinuities are expected [3]. For this incompressible case, however, it offers a higher resolution computation of the complex vortical structures inside and downstream of the dimple [3].

3.4.2 Time Discretization. This research utilized the “Iterative Time–Advancement Scheme”, similar to the better known Dual Time Stepping coupled solver scheme [3]. This implicit treatment eliminates the splitting error resulting from the use of the segregated solver, and maintains second order accuracy in time [3].

3.4.3 Boundary Conditions. The computational model utilized the following FLUENT[®] boundary settings, as shown in Fig. 3.10.

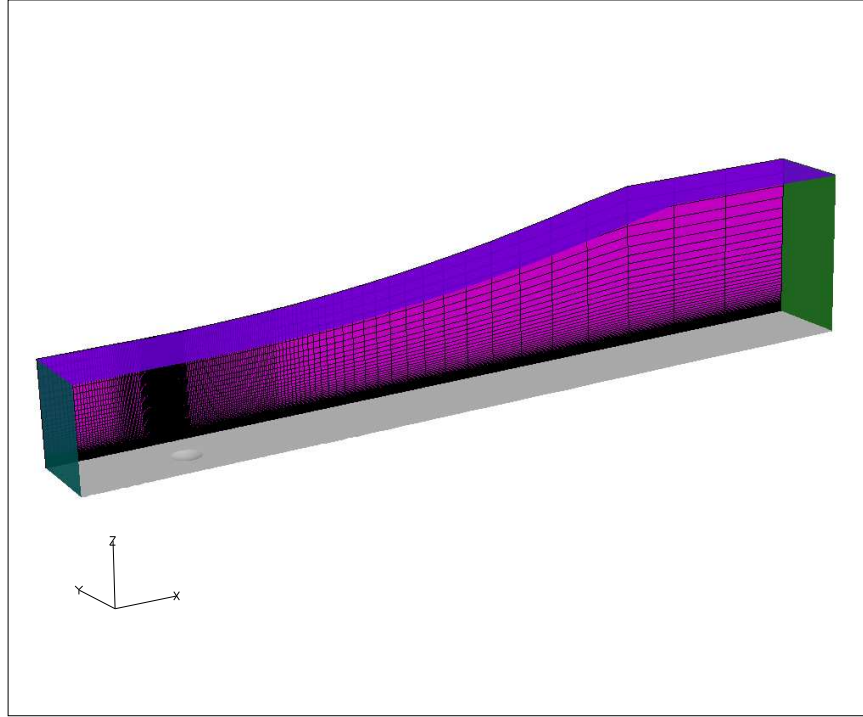


Figure 3.10: FLUENT® boundary conditions as applied to these models.

Blue	Velocity inlet = $10 \frac{m}{s}$
Purple	Wall, specified shear = 0
Green	Outflow
Gray	Wall, no slip
Magenta	Translational periodic boundary

3.5 Visualization

Through various visualizations and quantitative measurements of the flow solutions, a qualitative assessment is made of what structures exist inside the dimple and what they are doing/what effect they are having on the surrounding flow. For the visualization needs, this investigation relied heavily on FIELDVIEW® flow visualization software. The flow solution data is exported in the FIELDVIEW® unstructured data format, using the built-in translator in FLUENT, and read into FIELDVIEW®. The scalar quantities deemed most important for this analysis are: u (x-velocity), v (y-velocity), w (z-velocity), total pressure, helicity, x-vorticity, y-vorticity, z-vorticity and vorticity magnitude. FIELDVIEW® has the capability to make multiple iso-

surfaces of any scalar quantity, thresholded by any other scalar quantity. Using iso-surfaces and contours plotted on coordinate surfaces, many animations and still shots were made to discern what is happening in the flow. In addition to the iso surfaces, surface flows (oil flows) and a vorticity alignment/eigenmode analysis [19, 21] were performed to identify the vortical structures present in the flow [6].

The unsteady nature of the flow and the goals of this investigation demanded that the analysis involve animations. Snapshots in time, every 0.001 seconds, of the flow field were visualized with oil flows, vortex cores, lines of separation and reattachment and contours highlighting total pressure and vorticity. Then the snapshots were assembled into animations to discern the transient unsteady features of the flow. The animations range from 200 frames to 600 frames, representing 0.2 to 0.6 seconds of flow time respectively.

In addition to the stills and animations produced in FIELDVIEW[®], pressure probes were defined in FLUENT[®] along the channel centerline ($y = 0$) at $x = [0, 0.01, 0.05, 0.1, 0.15, 0.2, 0.3]$ locations and at $z = 0.001\text{m}$ off of the viscous wall. These probes provide data for the Power Spectrum Density plot and other analysis of the frequencies involved in the flow.

IV. Results

This research effort revealed that a wide variety of flows are present within the dimple cavity. Definite trends appear when the dimples are organized by Re_x and Re_D . These trends appear when looking at the the energy in the dimple flow structures, the organization and symmetry of the flow, the stability and structure of the vortex cores, the size of the recirculation zones, the presence and frequency of pressure waves, the presence of a ‘bulk’ shed of the pinned vortices and the downstream flow effects. Figure 4.1 explains how to interpret the diagrams depicting the dimple flow structures presented in this chapter. The basic elements presented with the dimples are: the surface or oil flow lines drawn in gray, the vortex cores (highlighted in green), the recirculation zone (highlighted in yellow) — bounded by the leading edge line of separation (highlighted in blue) and the trailing edge reattachment line

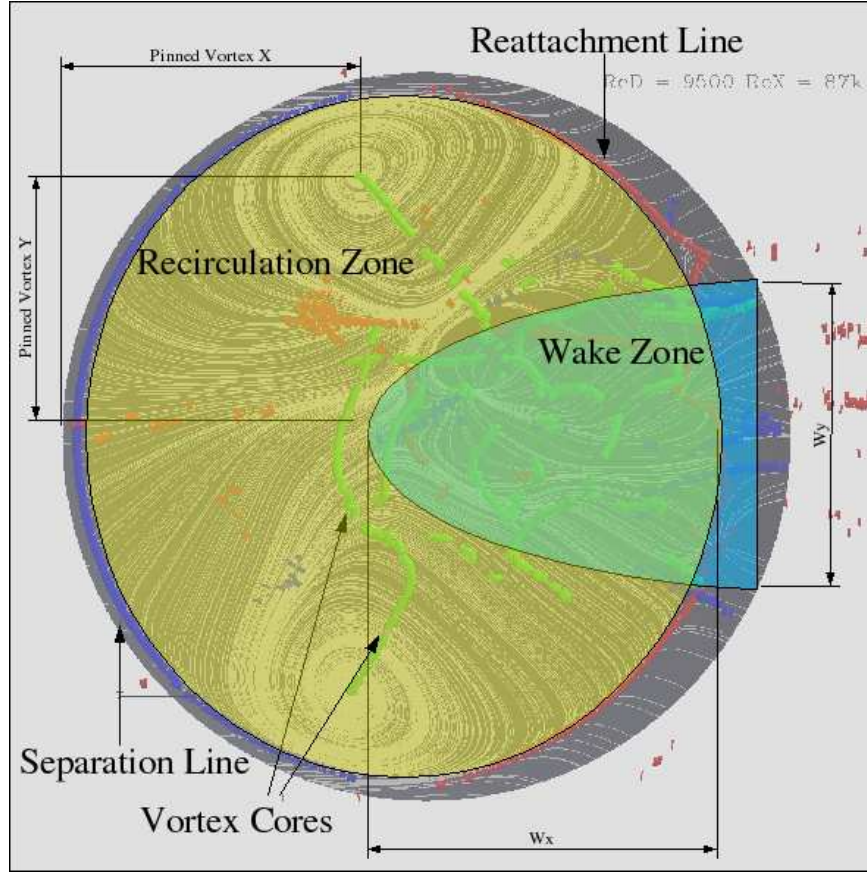


Figure 4.1: Dimple diagram legend.

(highlighted in red) and the wake zone — the region within the recirculation zone where the shedding vortices dominate the flow characteristics (highlighted in cyan).

4.1 *Energy in Flow Structures*

The measure of energy is a qualitative assessment based on the thickness of the boundary layer and the presented area of the dimple. The thicker the boundary layer, the farther away the high energy flow, and therefore the dimple experiences a lower energy flow. Likewise the smaller the dimple, the smaller area it has to draw in flow, and so therefore less energy flows through the dimple.

In Fig. 4.2, the progression becomes apparent. The red gradient in the background represents the energy in the flow. The upper left corner represents a relatively high energy case and the lower right corner a relatively low energy case. From the low energy ineffectiveness, to the chaos at the higher energy cases it is understandable how the effectiveness of the dimples could be targeted and limited to a specific energy regime. In the low energy case there is very little interaction between the dimple and the flow. In the higher energy cases, the chaos would certainly trip to turbulence and just be absorbed into the other turbulent flow eddies, also imparting relatively little change to the overall flow. It is interesting to recall that previous studies have shown that the dimples have a limited range of effectiveness, before and after which they cause relatively little change to the flow [2, 8, 10, 14, 20]. Figure 4.3 gives a closer look at nine of the cases presented in Fig. 4.2 allowing the structures more easily compared. The basic organization of Fig. 4.3 is identical to Fig. 4.2 in that the dimples are organized by Re_x in the x-direction and Re_D in the y-direction. The highly chaotic nature of the wake zones in 4.3(a), 4.3(b) and 4.3(d) distinguish these cases from the rest. This investigation identified these cases as the high-energy flow regimes. Similarly, the semi-organized structure of 4.3(c) and 4.3(e) — where the vortex cores are aligned and shedding in a parallel and periodic manner — leads them to be labelled as in transitional flow regimes. Finally the stable, pinned vortex

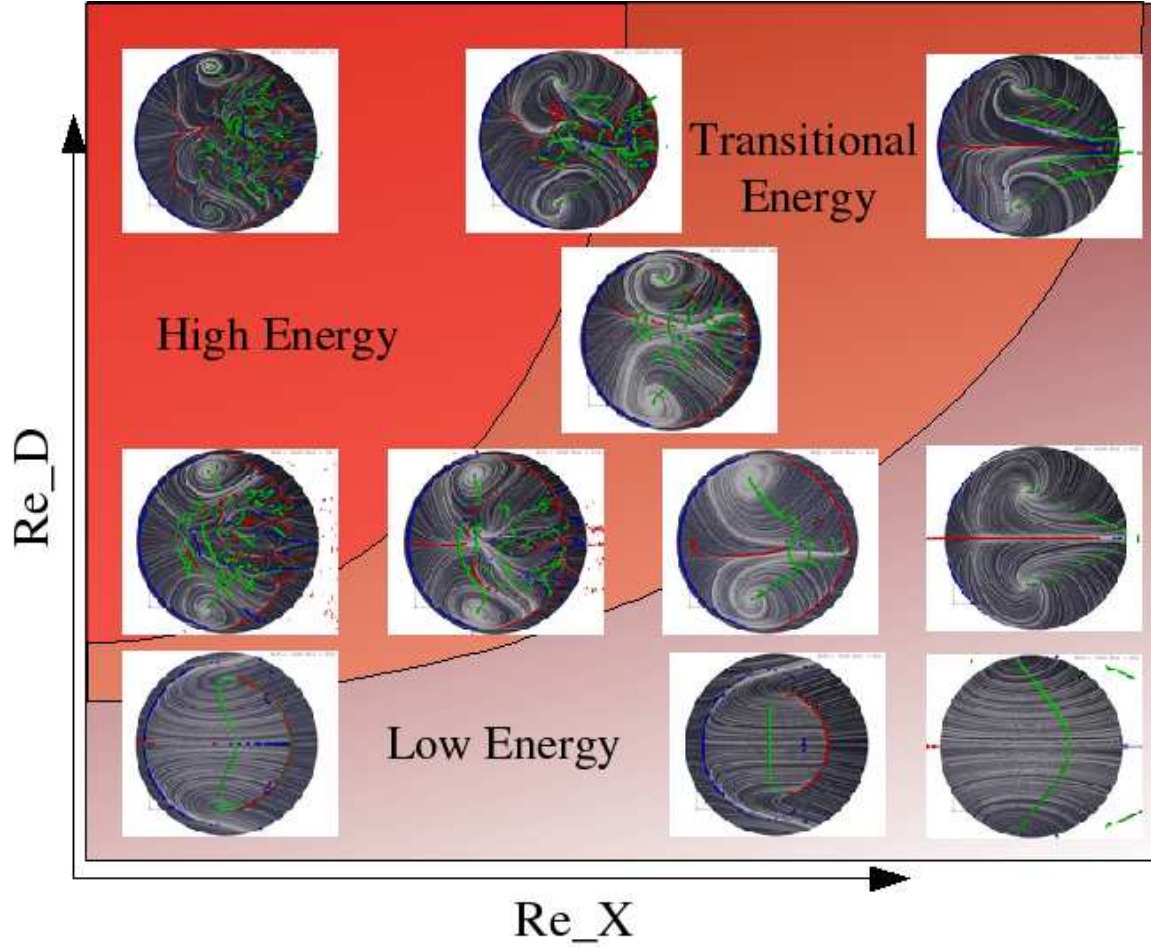


Figure 4.2: Energy graduation shown in the dimple flow structures. Dimples are organized according to the axes, energy is represented by the red gradient (Upper left corner is high energy and the lower right corner is low energy).

cores found in 4.3(f), 4.3(g), 4.3(h) and 4.3(i) identify them as falling into low-energy flow regimes.

4.2 Organization and Symmetry of Flow

Figure 4.3 presents a rough layout of the different flow structures seen in this investigation. Here the changing nature of the symmetry and organization of the flow is easily seen.

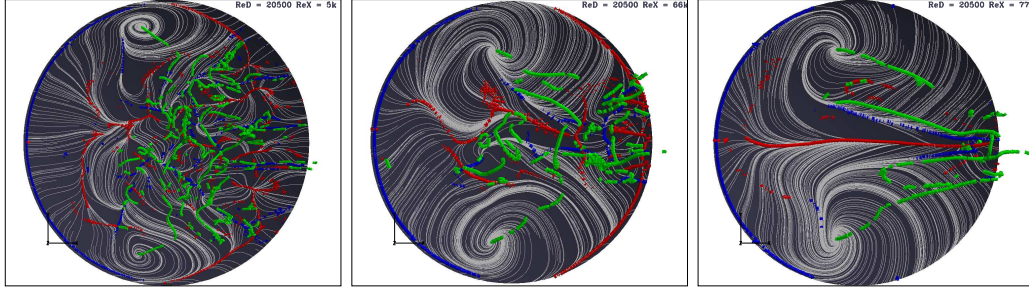
An obvious flow structure within the dimples is the vortex core at the center of the recirculation zone and pinned near the cross-flow edges of the dimple. The

data collected in this investigation suggests that the vortex strength relative to the boundary layer momentum is what allows the trapped nature of the vortices at high Re_x and low Re_D , and likewise is directly related to the shedding structures at the lower Re_x values. For the purpose of qualitative comparison, the vortex strength is tied with its stability or ‘completeness’. This feature is measured primarily by the length of the pinned portions and the spanwise extent of the wake region.

The high-energy cases have a near chaotic wake region in their centers where this vortex structure is highly disorganized. As the energy decreases into the transitional energy realm, the wake region becomes much more organized and the cores are forming in a very organized fashion. Finally, in the low energy cases, the wake region disappears and symmetry is restored to the flow.

The most complete vortices are found in the low-energy cases where the boundary layer is thick or the dimple size is very small. In these cases, the low energy boundary layers or the small presented areas and recirculation zones — leave the vortices relatively strong and able to maintain continuity from pin to pin. As the dimple size increases, the presented area of the dimple increases — increasing the inflow of energy. Likewise a larger dimple has a larger recirculation zone area. The data suggests that the greater amount of boundary layer energy acting on the larger recirculation zone area causes the vortices to break off of the pinned portions and form the wake zone.

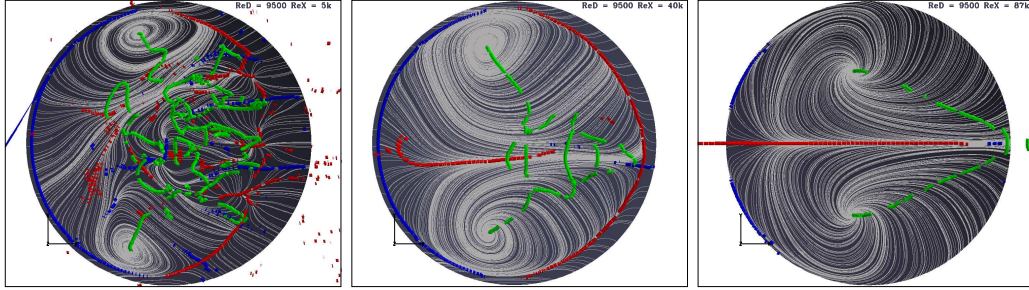
It is significant to understand that outside of the low energy realm, symmetry does not apply. This is significant because there are many published CFD models of dimples that assumed and used a line of symmetry down the centers of the models well outside of this low-energy symmetric region [10–12].



(a) $Re_D = 20500, Re_x = 5000$

(b) $Re_D = 20500, Re_x = 60000$

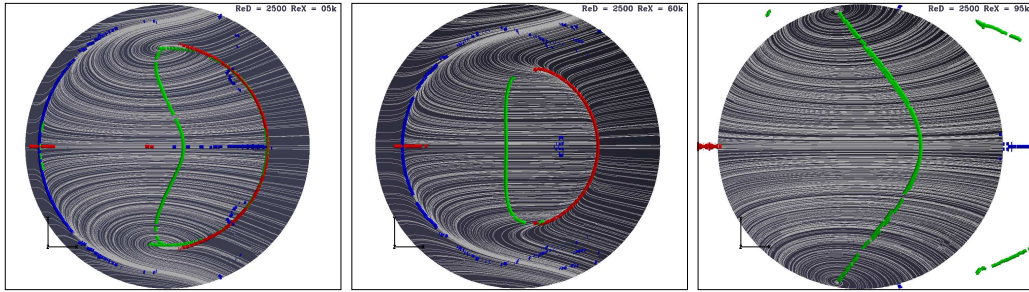
(c) $Re_D = 20500, Re_x = 77000$



(d) $Re_D = 9500, Re_x = 5000$

(e) $Re_D = 9500, Re_x = 40000$

(f) $Re_D = 9500, Re_x = 87000$



(g) $Re_D = 2500, Re_x = 5000$

(h) $Re_D = 2500, Re_x = 60000$

(i) $Re_D = 2500, Re_x = 95000$

Figure 4.3: Variations of Re_x over constant Re_D

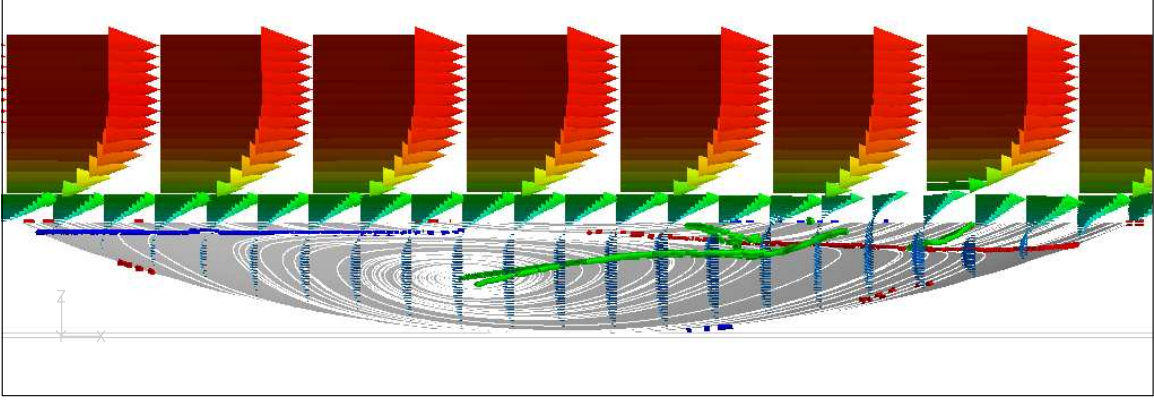


Figure 4.4: Inner dimple vortex structure.

4.3 Size of Recirculation and Wake Zones

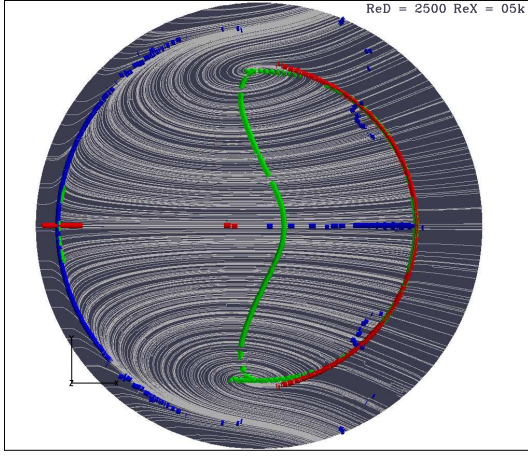
The recirculation zone, as mentioned before, is bounded by the separation line on the upstream side and the reattachment line on the downstream side. Within this zone, the velocity along the wall is directed upstream, creating the vortex core at the interface between the upstream flow and the downstream flow. In Fig. 4.4 the velocity vectors highlight this primary inner dimple structure.

In Fig. 4.3, it is apparent that as Re_x increases, the wake region grows smaller. The size of this region is directly related to the shear layer imposing its velocity gradient on the recirculation zone. When the gradient and interface areas are sufficiently large (high Re_D and low Re_x) the vortex cannot remain trapped and sheds off its mid section. For the purpose of qualitatively analyzing this behavior, the distance between the pinned vortex sections represents the size or rather extent of this wake region in the Y-direction of our sample space, W_y in Fig. 4.1.

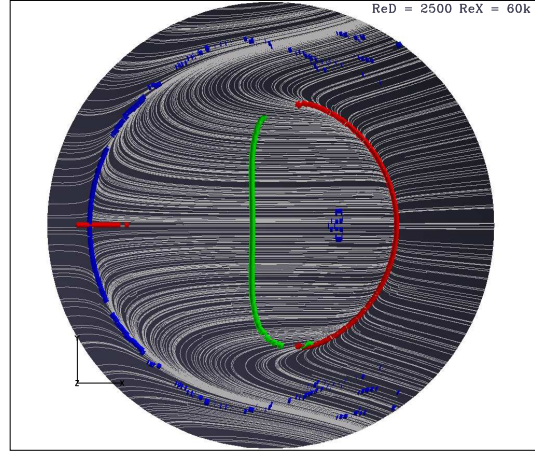
Within the high-energy wake region the vortex cores appear nearly chaotic. This transition to chaos with increasing energy most likely is the mechanism that allows the dimples to become invisible to high Re flows [11, 14, 20]. As energy increases beyond the high-energy regime tested here, the flow would certainly trip turbulent and the vortex pieces in this wake zone would simply intermingle with the turbulent eddies and render the dimple invisible.

In the transitional energy regimes, this wake region changes its appearance dramatically. The chaotic state of the vortex cores in the high-energy wake zone gradually organize into parallel vortices at regular intervals. The return to order is also apparent when looking at the oil flow lines and the lines of reattachment and separation. The oil flow loses its chaotic appearance entirely and forms smooth continuous lines highlighting the primary vortex swirl. As well, the reattachment line along the trailing edge of the dimple regains its continuity.

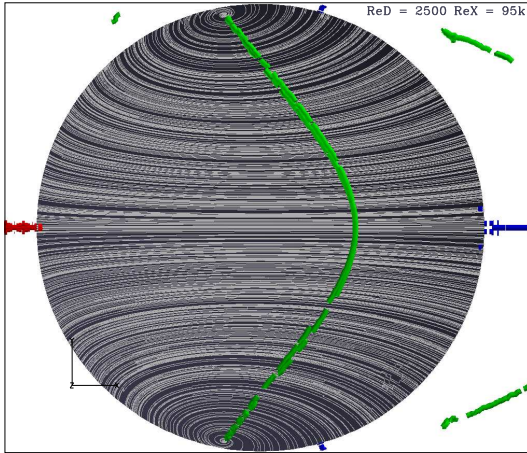
In the low energy flows, all of the cases showed a symmetric and stable flow structure. In Fig. 4.5, the small dimple is presented at all boundary layer conditions. Here it is interesting to see the symmetry and the sizes of the recirculation zones. In the lowest energy case the vortex in the dimple was able to grow beyond the boundaries of the dimple and essentially act as a fixed separation bubble at the baseline separation line.



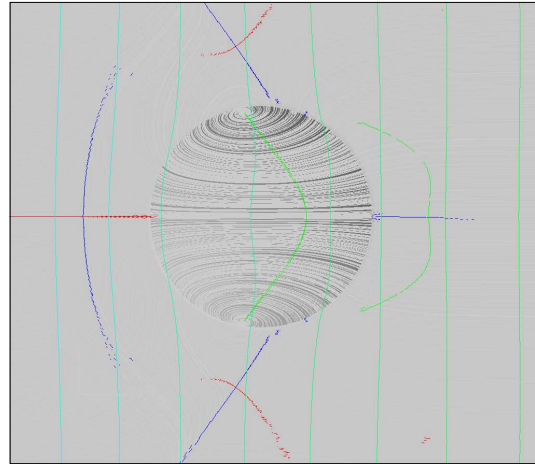
(a) $Re_D = 2500, Re_x = 5000$



(b) $Re_D = 2500, Re_x = 60000$



(c) $Re_D = 2500, Re_x = 95000$



(d) $Re_D = 2500, Re_x = 95000$ showing the growth in the recirculation zone

Figure 4.5: Snapshots of the flow structures showing trapped vortices and low-energy recirculation zone flow.

4.4 *Frequency of Pressure Waves*

As the shedding vortices collide with the trailing edge of the dimple, they create a phenomenon similar to waves crashing on the shore as seen in Fig. 4.6(top). Here the waves in the velocity vectors are highlighted by contours of total pressure (top) and a carefully selected iso-surface — in orange (bottom). These waves shed at a regular frequency, which can be counted visually through the animations of the flow, and verified through the reduction of pressure tap data using a PSD plot.

4.4.1 Frequency analysis. The frequencies recorded were originally found through animations and then later supported by running a PSD on pressure tap data from the flow field. The numbers were in perfect agreement for the high frequency oscillations. The lower frequency bulk flow oscillations were either buried in the average flow noise around $0.0Hz$ or their magnitudes were so small that they remained undetectable on the PSD.

The baseline shedding frequencies can be seen in Fig. 4.7 and Fig. 4.8. The primary shedding frequency for the baseline case is $\approx 90Hz$. This frequency remains visible on most of the PSD plots. Figures 4.9 and 4.10 show the pressure wave variations and frequencies for the largest dimple with the smallest boundary layer — the highest energy case. In Fig. 4.10 the frequency spike at $\approx 520Hz$ is caused by the high frequency primary vortex shedding and can be seen in the animations, Fig. 4.11. The pressure waves remain very tangible and their frequencies relatively constant for all of large dimple cases, but in the medium dimple cases the frequencies change dramatically.

Figures 4.12 through 4.14 show the medium dimple with the smallest boundary layer. This is still a high-energy case, but the frequency is less than half of the large dimple case. The frequency spike at $\approx 250Hz$ in Fig. 4.13 correlates with the visualization in Fig. 4.14. In these high-energy medium-dimple cases, the pressure waves bifurcate and form two separate structures travelling downstream parallel to one another, as seen in Fig. 4.14.

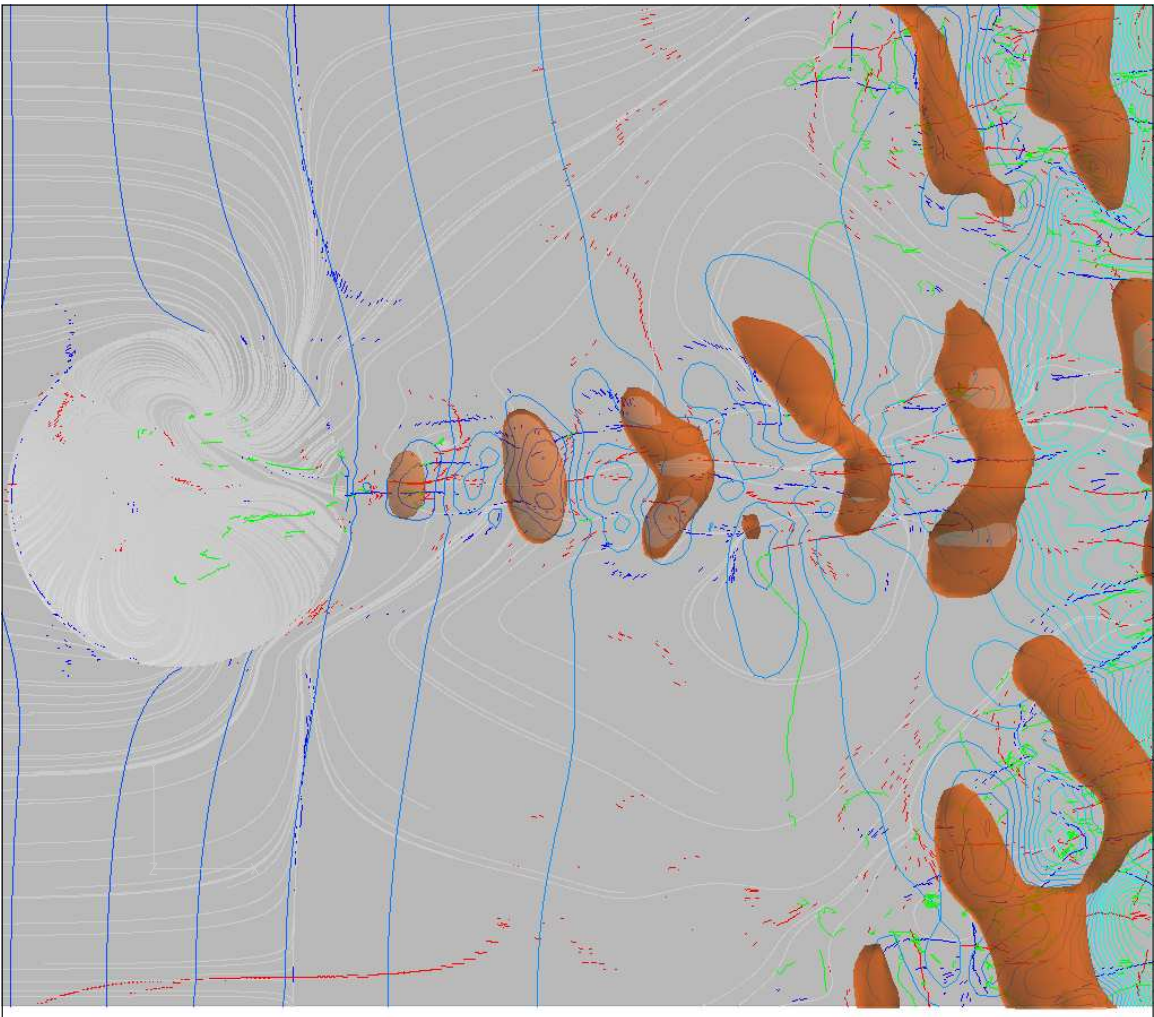
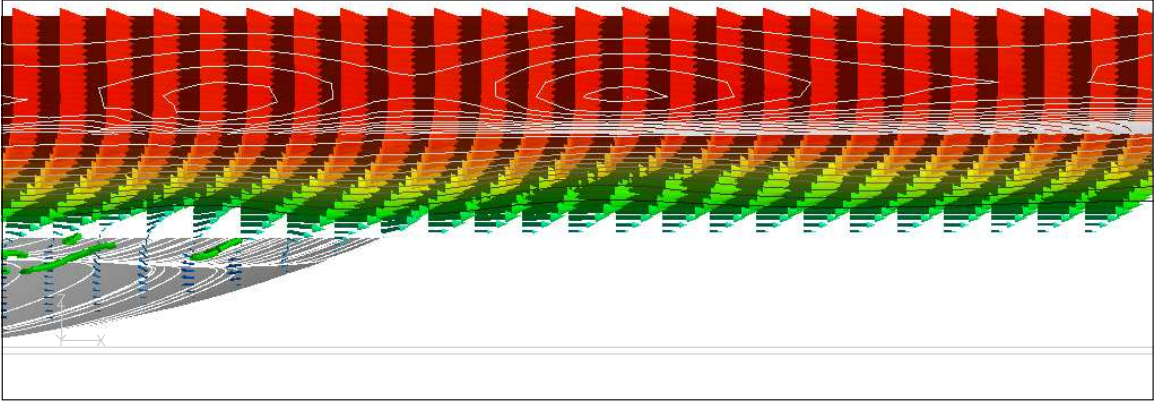


Figure 4.6: Shedding vortices produce pressure waves (top) shown in contours in freestream flow, (bottom) shown in orange iso-surfaces of pressure.

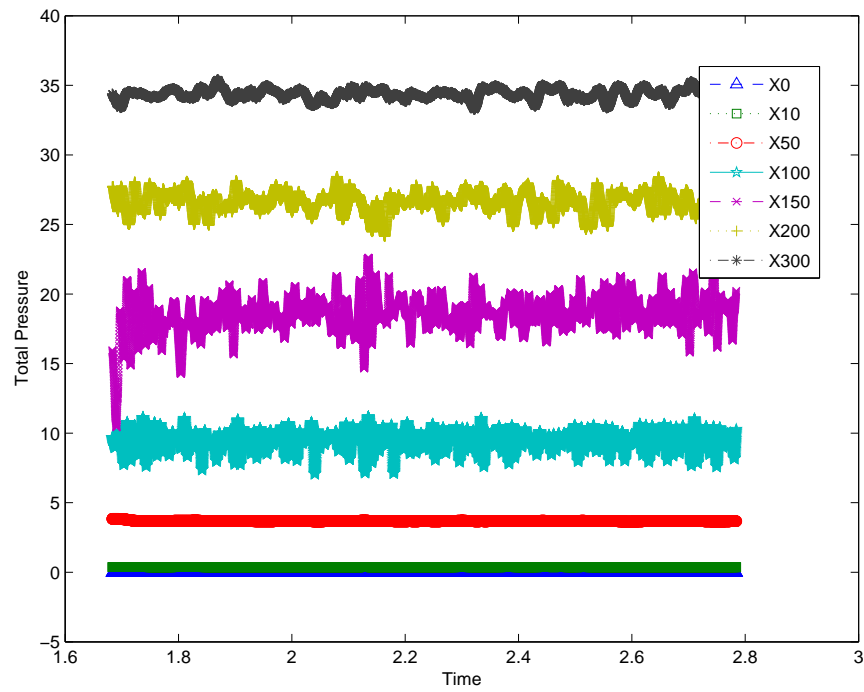


Figure 4.7: A portion of the pressure tap data for the baseline channel from which the PSD was calculated.

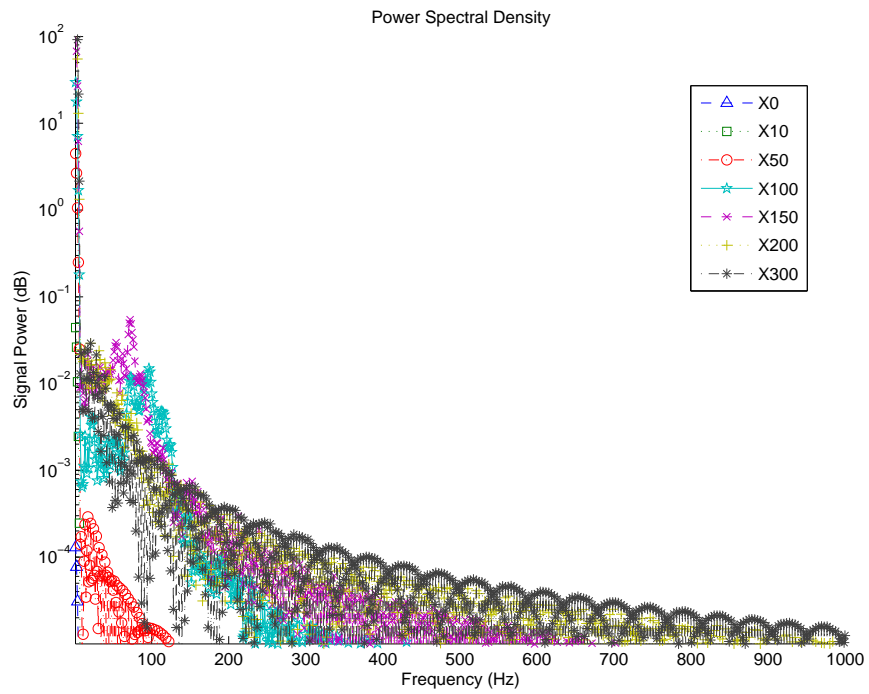


Figure 4.8: PSD for the pressure data from the baseline channel.

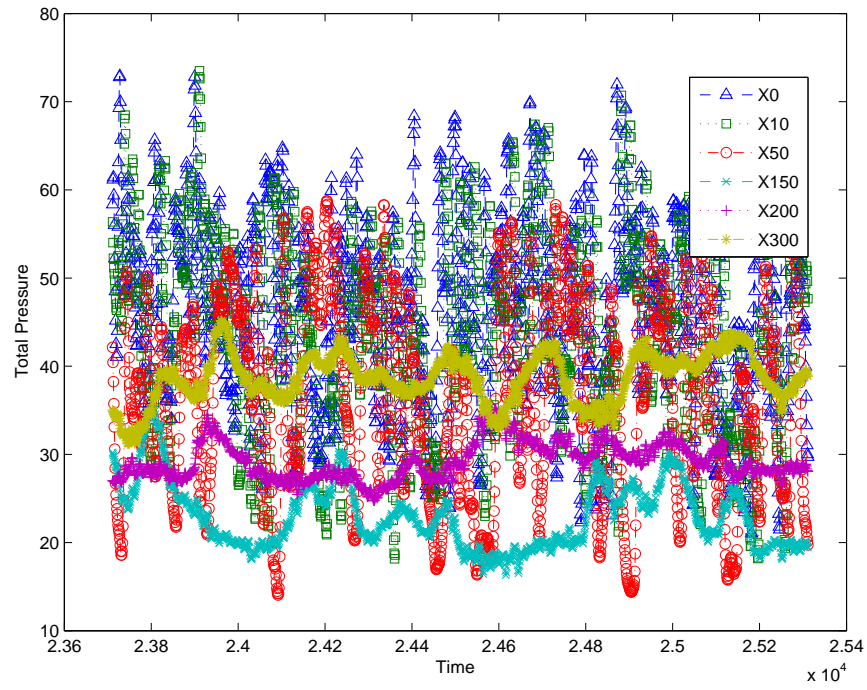


Figure 4.9: A portion of the pressure tap data for $Re_D = 20500$ $Re_x = 5000$ from which the PSD was calculated.

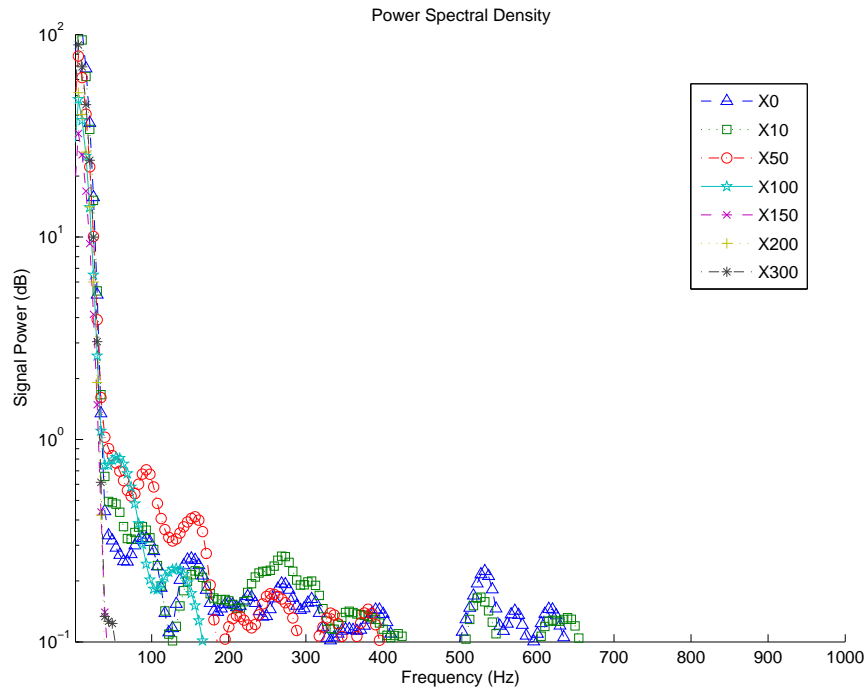


Figure 4.10: PSD for the pressure data from $Re_D = 20500$ $Re_x = 5000$.

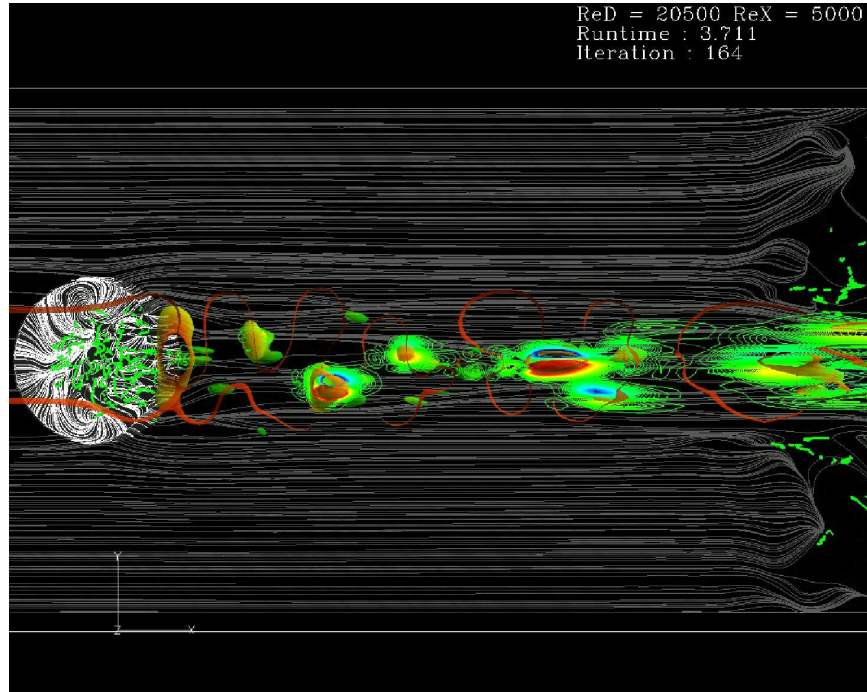


Figure 4.11: Visualization of pressure waves (still frame from animation) $Re_D = 20500$ $Re_x = 5000$.

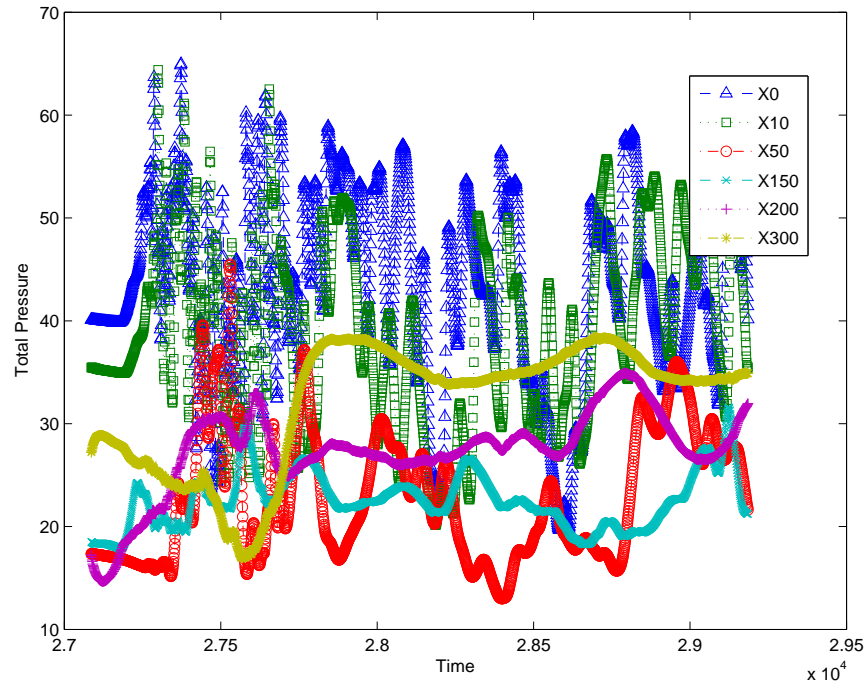


Figure 4.12: A portion of the pressure tap data from which the PSD was calculated.

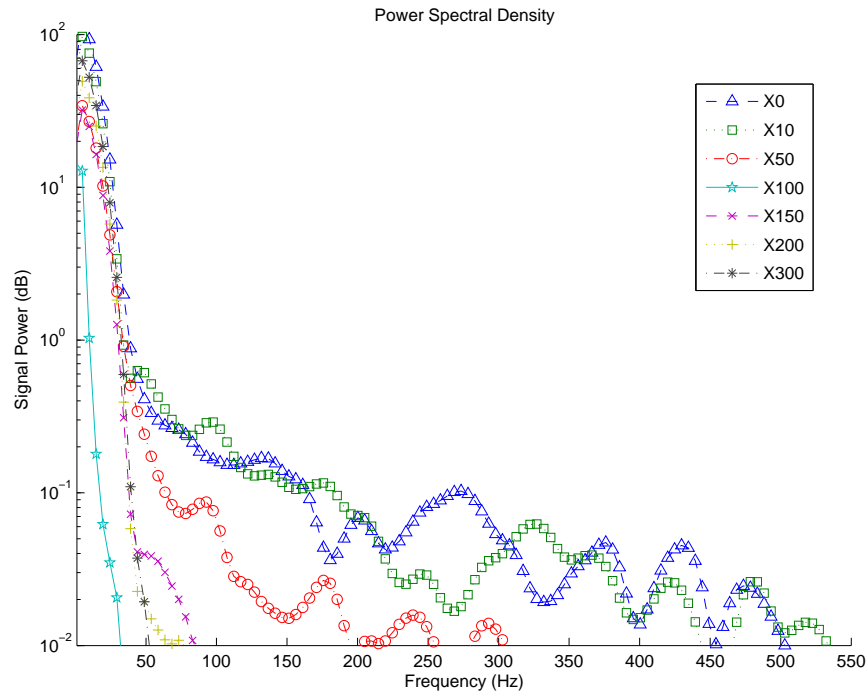


Figure 4.13: PSD for the pressure data from $Re_D = 9500$ $Re_x = 5000$.

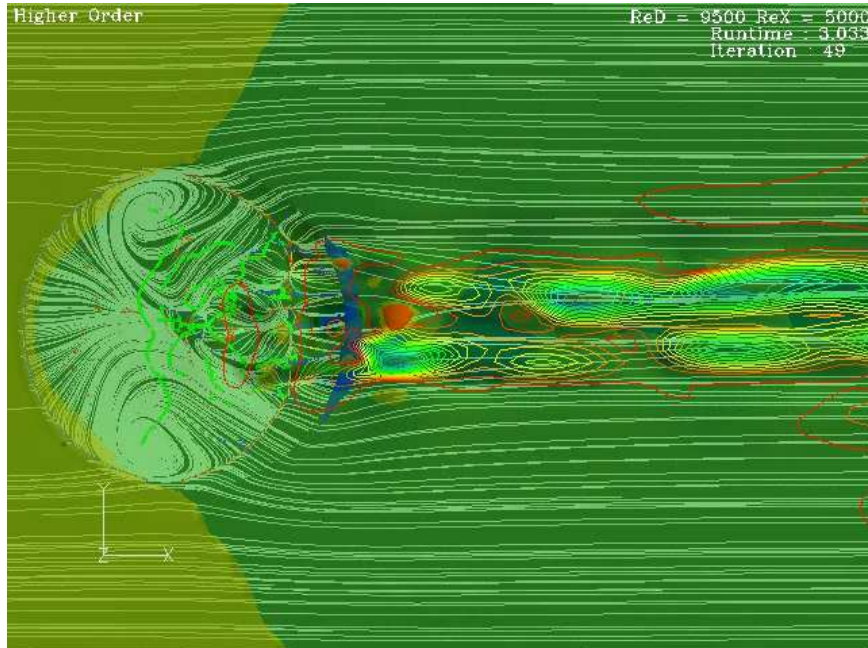


Figure 4.14: Visualization of pressure waves (still frame from animation) $Re_D = 9500$ $Re_x = 5000$.

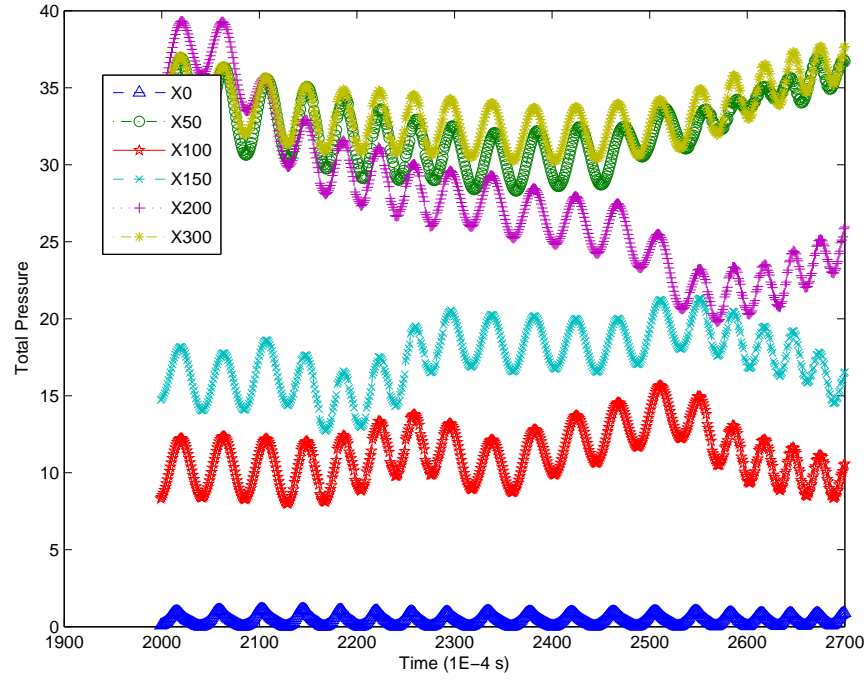


Figure 4.15: A portion of the pressure tap data from which the PSD was calculated.

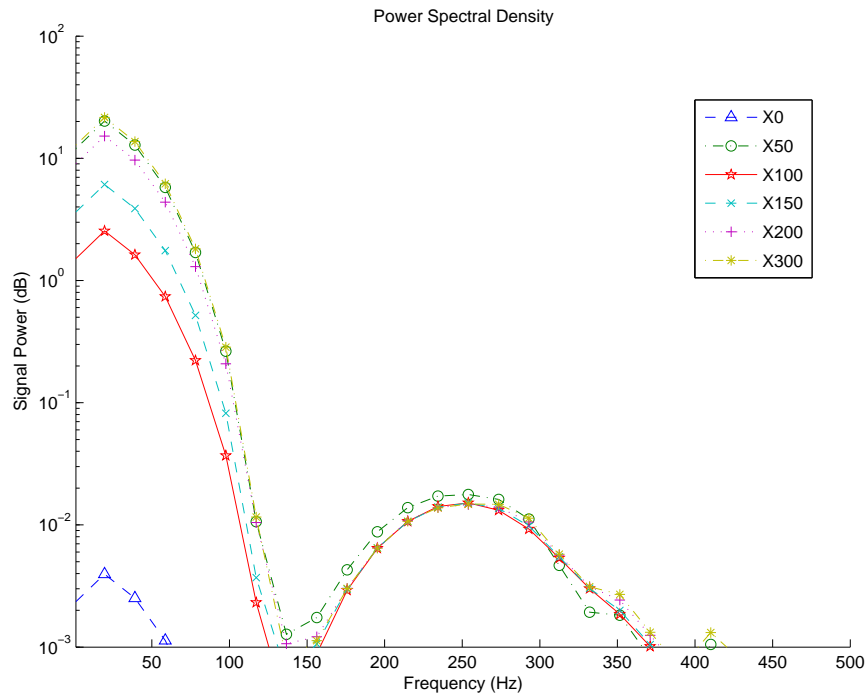


Figure 4.16: PSD for the pressure data from $Re_D = 9500$ $Re_x = 40000$.

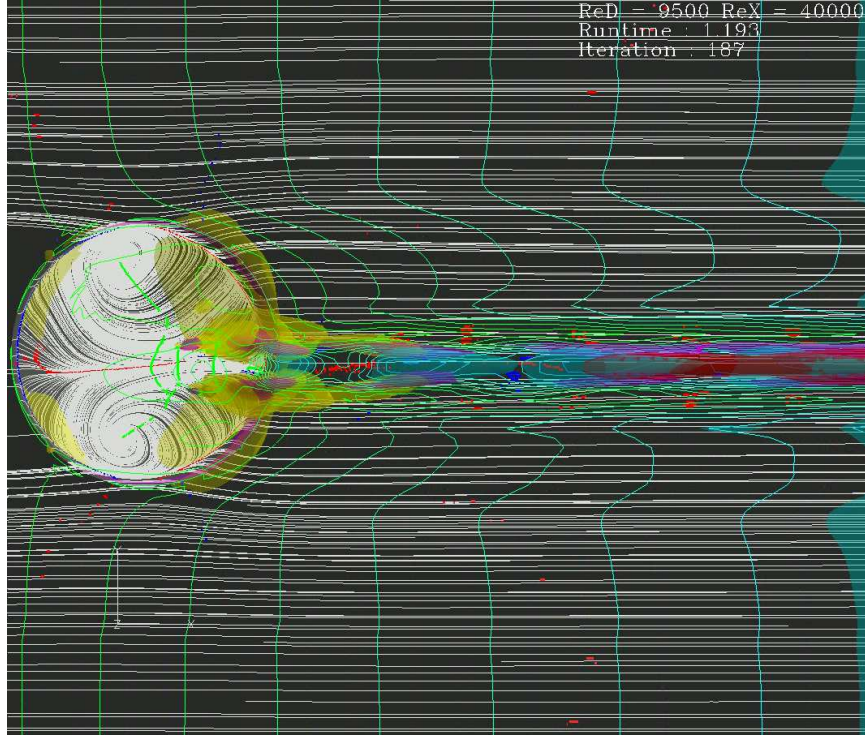


Figure 4.17: Visualization of pressure waves (still frame from animation) $Re_D = 9500$ $Re_x = 40000$.

Figures 4.15 through 4.17 show the medium dimple with a medium boundary layer. This is a transitional energy case, here the frequency still nearly matches that found in the high-energy medium-dimple case. The frequency spike at $\approx 250Hz$ in Fig. 4.16 correlates with the visualization in Fig. 4.17. At this energy level the pressure differences (contour lines) are not as well defined so the visualizations also utilized iso-surfaces of vorticity to make the features more apparent. In this case the shed vortices remain on the centerline and abandon the bifurcated structure of the higher energy cases of this dimple size. This case is roughly equal to the case that Khalatov et. al [9] determined to be most effective. It is interesting that this case alone exhibits the propagation of its high frequency to all of the pressure probes, Fig. 4.15.

The close relationship between the dimple size and the frequency of this primary shedding suggests that the frequency is primarily dependent on dimple diameter alone. In the large dimple cases the frequency fluctuates $\pm 5\%$ with variations in Re_x . When

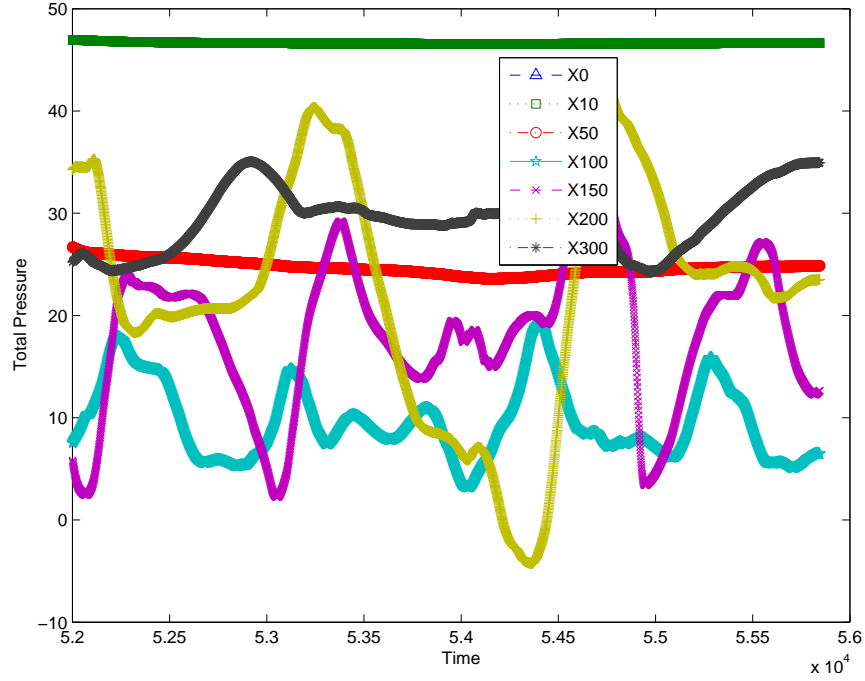


Figure 4.18: A portion of the pressure tap data from which the PSD was calculated.

the dimple size changes, however, the frequency changes nearly proportional to the diameter change. The large dimple had a frequency $\approx 520Hz$ for $Re_D = 20500$, the medium dimple had a frequency $\approx 250Hz$ for $Re_D = 9500$. The ratio of frequencies is less than 4% different than the ratio of Re_D .

Figures 4.18 and 4.19 show the small dimple with a medium boundary layer. This is a low-energy case. There is no detectable shedding or oscillating pressure. The frequencies shown in Fig. 4.19 correlate with the visualization in Fig. 4.20, no frequencies outside of the basic flow noise were detected.

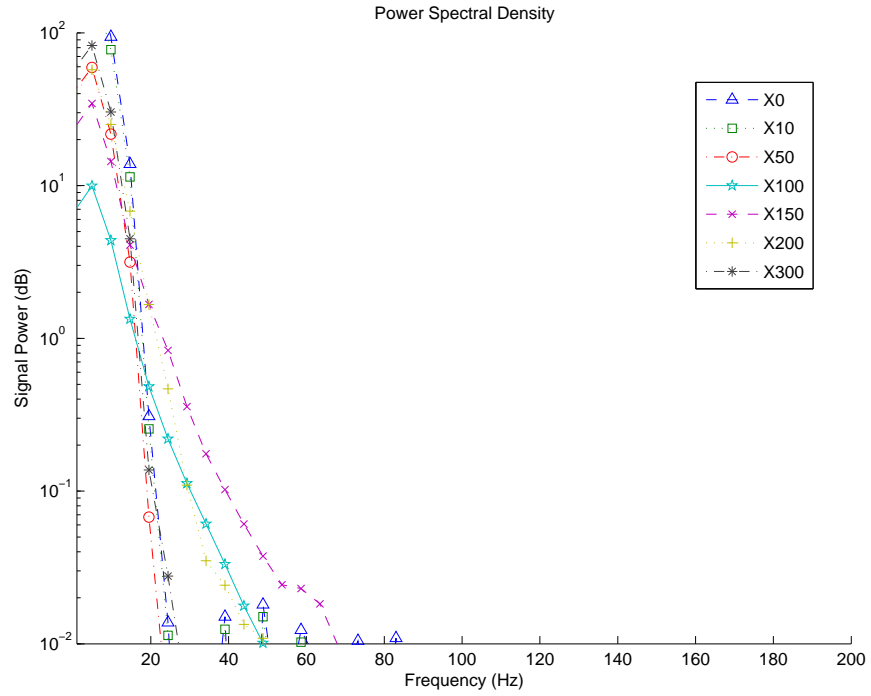


Figure 4.19: PSD for the pressure data from $Re_D = 2500$ $Re_x = 60000$.

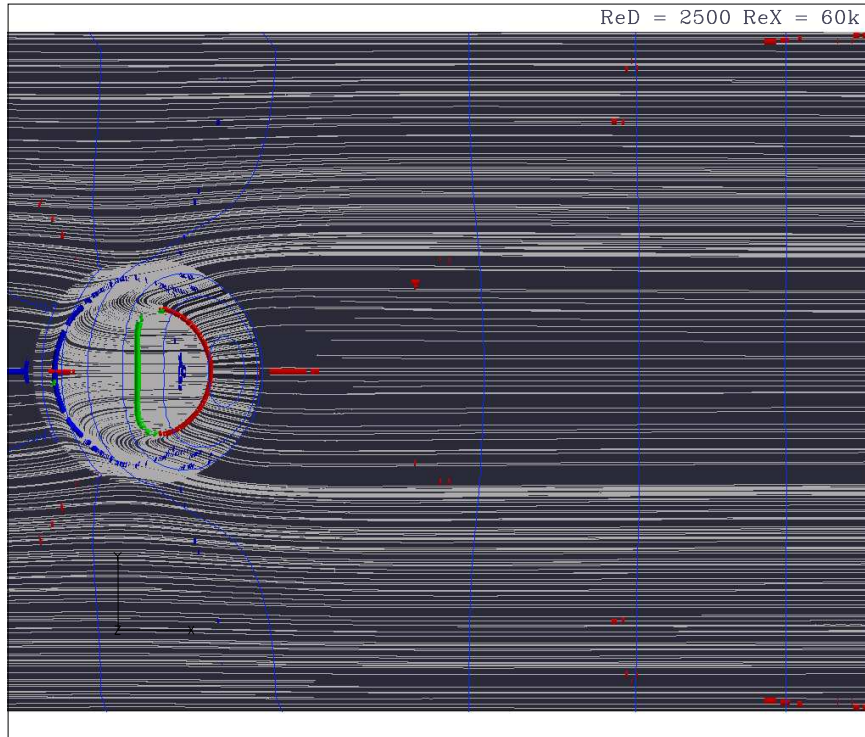
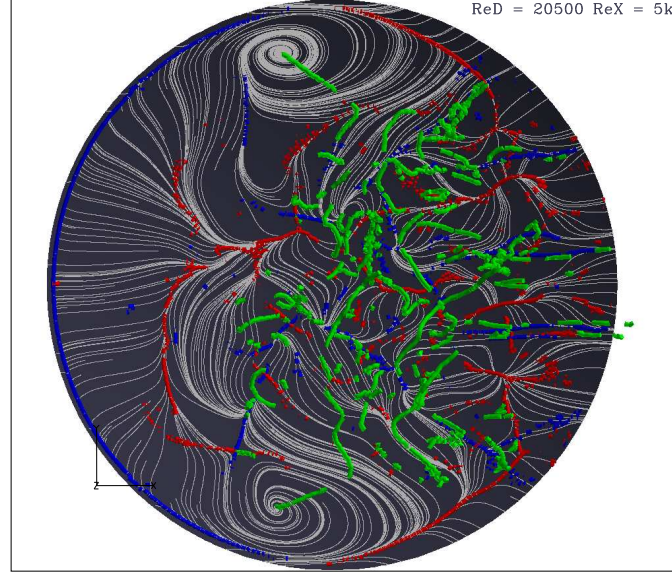


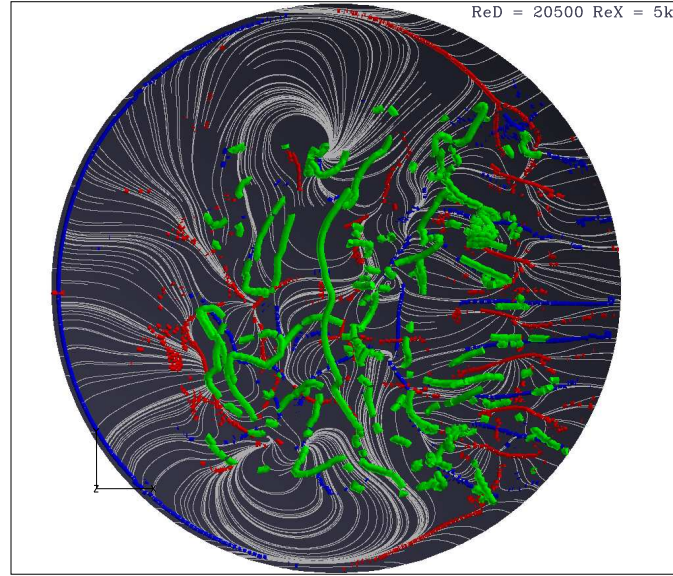
Figure 4.20: Visualization of pressure waves (still frame from animation) $Re_D = 2500$ $Re_x = 60000$.

4.4.2 *Bulk Shed Phenomena.* Another phenomenon critical to understanding the dimple's passive relationship to the environment is the periodic total shed of the entire vortex structure within the dimple. The high-frequency shedding of vortices is not absolutely periodic within the dimple. The vortex cores form in irregular intervals but then coalesce on their impingement on the dimple trailing edge. The resulting coalesced vortices turn into the highly periodic waves seen in the visualizations and analysis in Section 4.4.1. This coalescing and shedding process causes another instability within the dimple which looks like a filling/dumping or 'breathing' cycle. The breathing of the dimple causes the pinned ends to walk in circles around their respective average pin points. This movement periodically moves the entire vortex into the more vulnerable high-energy wake region in the middle of the dimple and causes the pinned ends to shed. This relationship, though straight forward, does not correlate with changes to the higher shedding frequency. In Fig. 4.21, a snapshot is shown of a dimple in the stabilized form and then immediately after a shed. Only the higher-energy dimples exhibited this flow characteristic. In animations the bulk shed corresponded with a larger downstream effect due to the momentary increase in mass flow out of the dimple. As the energy involved decreases, the flows transition from simultaneous periodic sheds of the pinned vortices to an alternating side to side shedding more typical of a Karmen street. An example of this is shown in Fig. 4.22(b). The bottom vortex has just shed off, but the top vortex remains clearly pinned. Interestingly, the bulk shed seems to be more than just a function of the energy that has been previously discussed. Figure 4.23 shows the large dimple in a thick boundary layer. Here the upper pinned vortex is about to shed, but in this case a new vortex that is building in the middle will replace the upper vortex almost instantly following the shed. Figure 4.24 presents the high-energy medium-dimple which also experiences the side to side shedding. The lower-energy medium-dimple cases do not experience any bulk shedding. They do maintain a fluctuation in the pin locations of the pinned vortices that highlights the breathing action of the dimples.

This breathing causes the surrounding stream lines to fluctuate as well, but was not detectable through the PSD analysis of the flow field pressure taps.

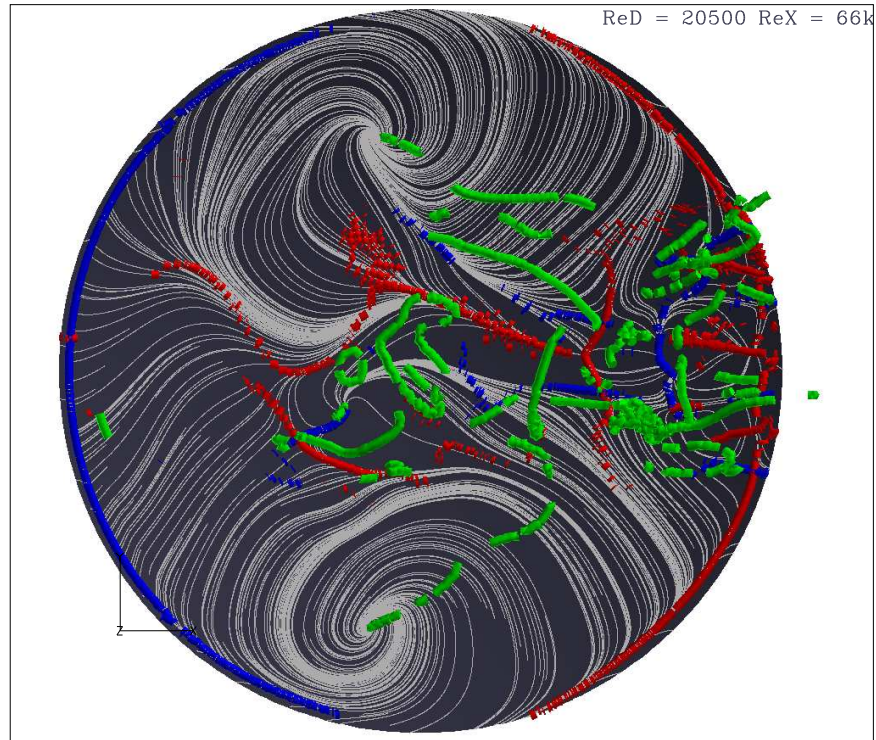


(a) Close up of the case $Re_D = 20500$ $Re_x = 5000$

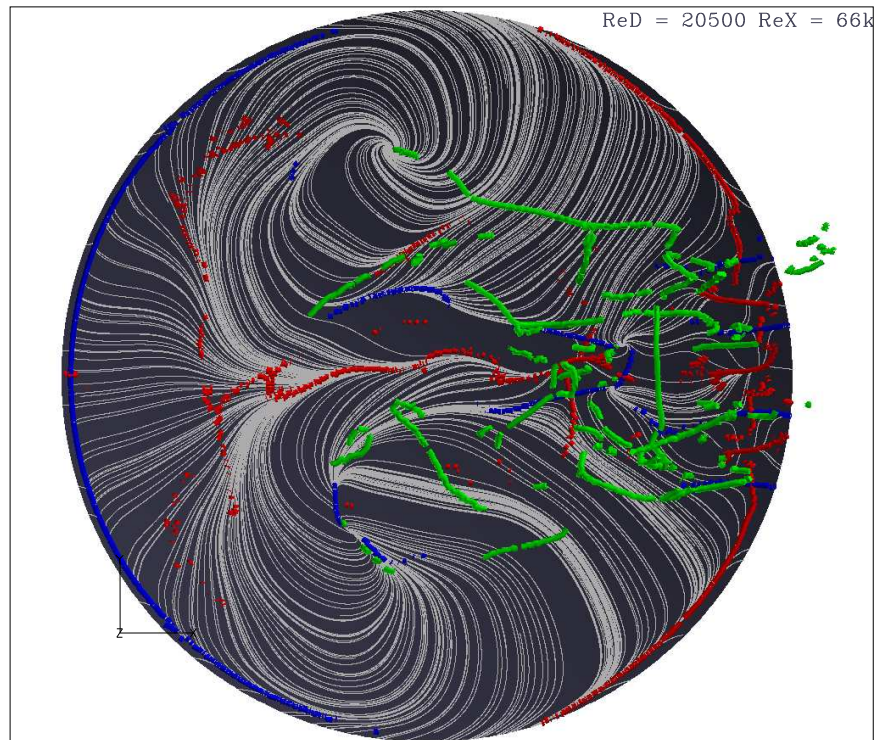


(b) Close up of the case $Re_D = 20500$ $Re_x = 5000$
after a bulk shed of pinned vortices

Figure 4.21: Snapshots of the flow structures showing unsteadiness and the 'Bulk Flow' feature.



(a) Close up of the case $Re_D = 20500$ $Re_x = 66000$



(b) Close up of the case $Re_D = 20500$ $Re_x = 66000$ after a bulk shed from bottom vortex

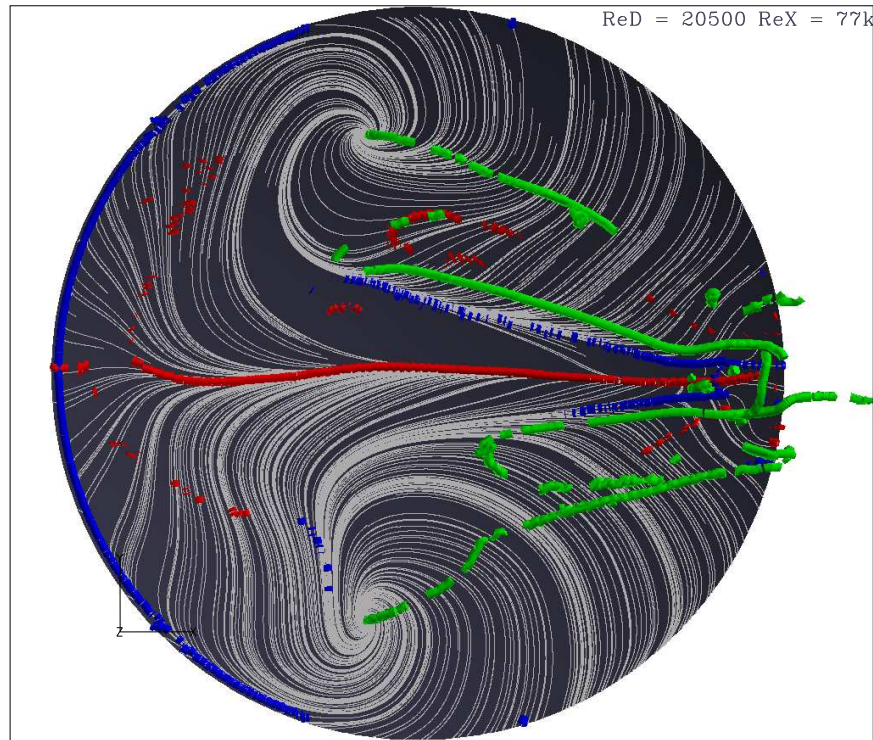
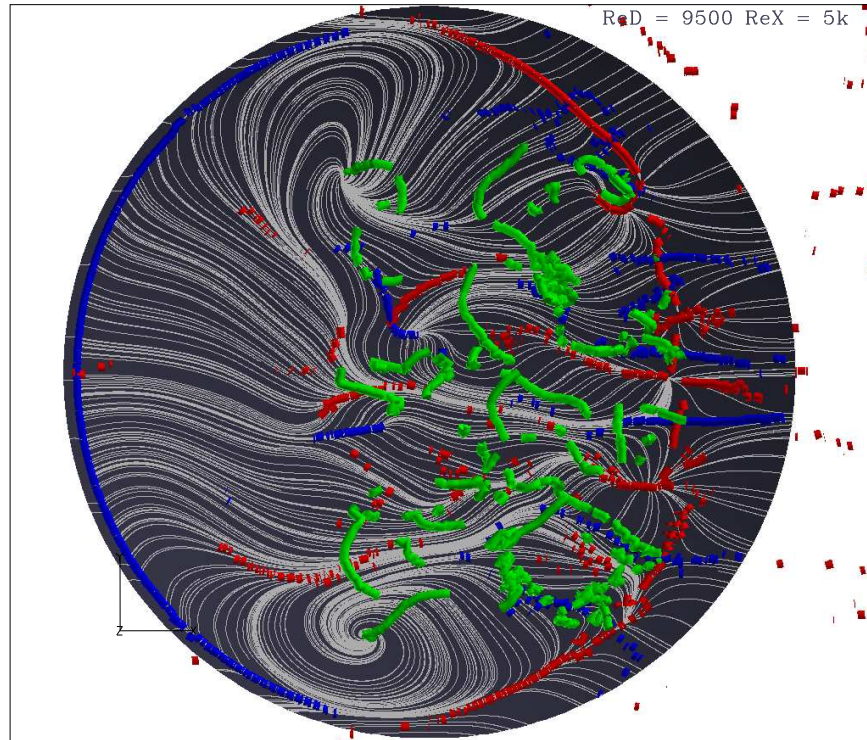
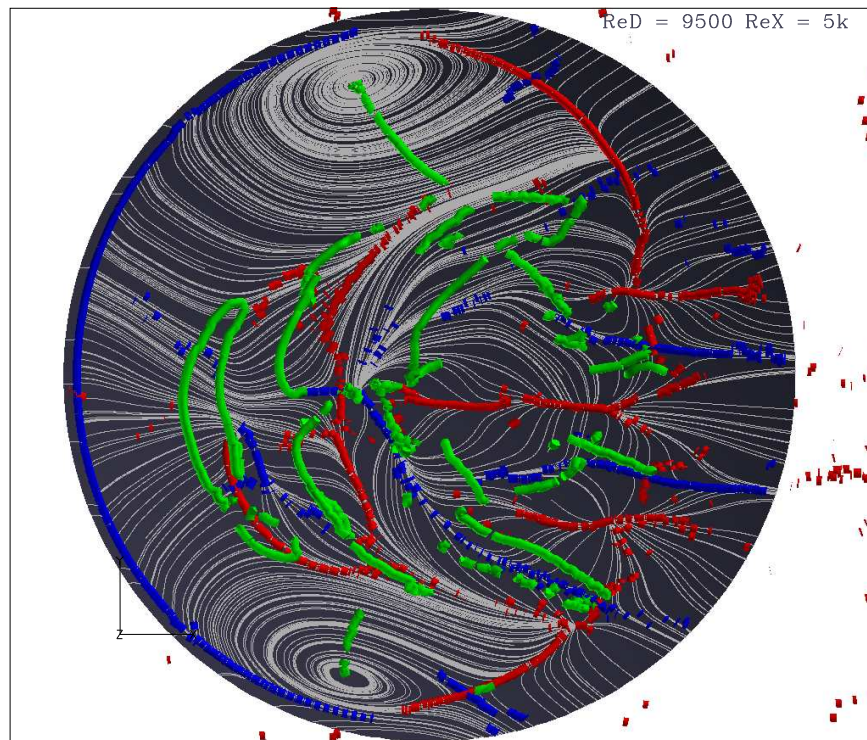


Figure 4.23: Close up of the case $Re_D = 20500$ $Re_x = 77000$ with clearly formed edge vortices.



(a) Absence of organized structures within dimple immediately following the complete shed of the pinned vortices

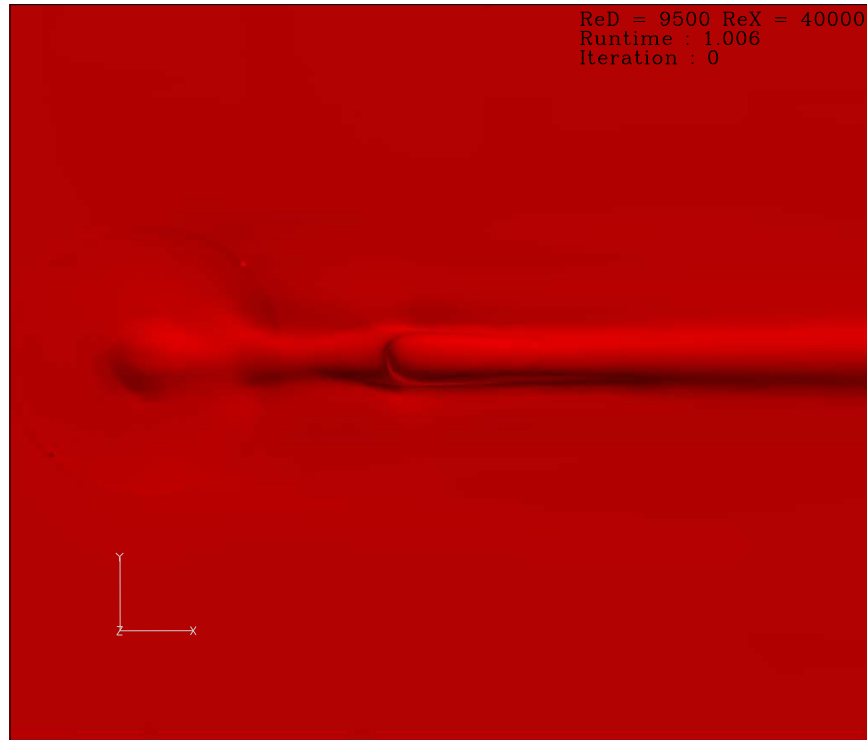


(b) Recovered flow structures resumed high-frequency central vortex sheds

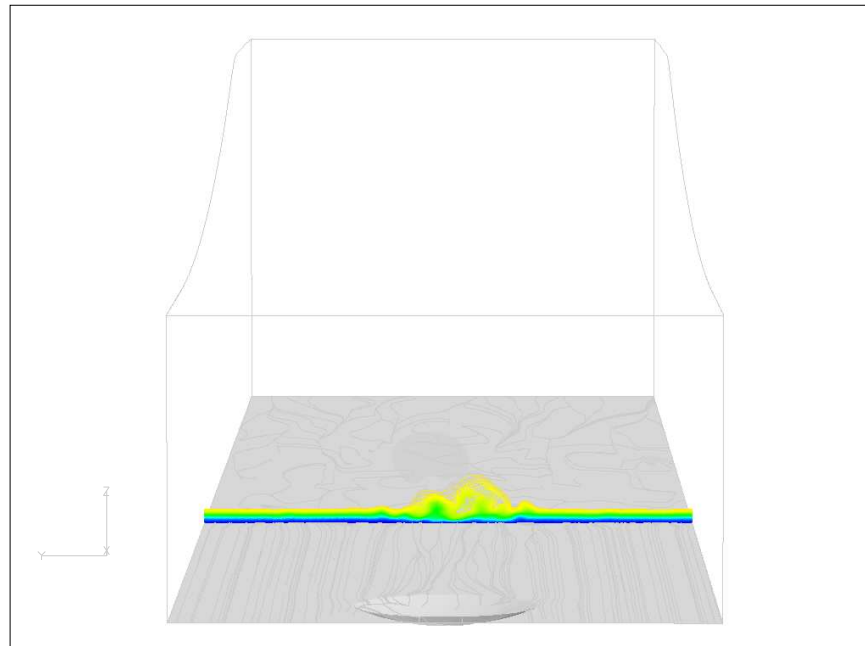
4.5 Downstream Flow effects and Mixing

The dimple has the passive effect of mixing the low energy boundary layer flow up into the higher energy free-stream flow. The transport mechanism is dominated by the complex vortical structures within and trailing after the dimple. An iso-surface of total pressure is seen in Fig. 4.25.a and the contours of U-velocity ($= [0, 99\% U_\infty]$) seen in Fig. 4.25.b show how dramatic this effect can be. In Fig. 4.25.b the boundary layer is nearly three times larger than the relatively unaffected regions outside of the dimple wake. Also interesting to note is the velocity distribution within the boundary layer. The low-velocity wall region is dramatically reduced, while the higher velocity, near-free-stream part is significantly increased, again pointing to the fact that mixing is occurring. Figures 4.26 through 4.32 depict the changing flow effects on the u-velocity as the energy levels change in the dimples. The high energy dimples are represented in Figs. 4.26, 4.27, 4.28 and 4.29. The transitional energy cases are depicted in Figs. 4.30 and 4.31. And a low energy case can be seen in 4.32.

The high-energy cases show the most dramatic activity, Fig. 4.26 shows the boundary layer in the dimple wake growing more than 5x that of the relatively undisturbed flow. Also interesting is that the more dramatic features of this growing boundary layer continue to grow with downstream distance. These features are consistent through all of the high-energy cases, Figs. 4.27, 4.28, and 4.29, though as the energy decreases the extreme nature of the effects also diminish.



(a) Iso-surface of total pressure



(b) Contours of u-velocity

Figure 4.25: Down-stream mixing region for the dimple, the max contour is at δ_{99} .

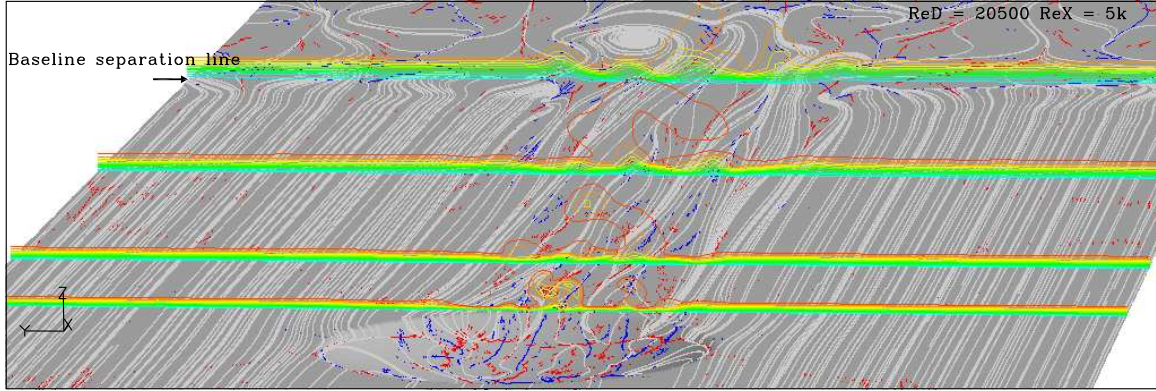


Figure 4.26: Downstream look at contours of u-velocity for $Re_D = 20500$ $Re_x = 5000$. Top contour represents u_{edge}

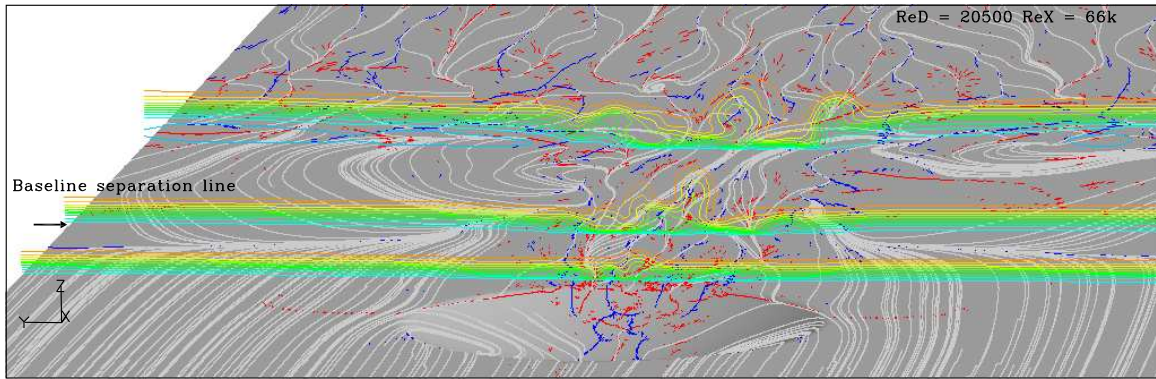


Figure 4.27: Downstream look at contours of u-velocity for $Re_D = 20500$ $Re_x = 66000$. Top contour represents u_{edge}

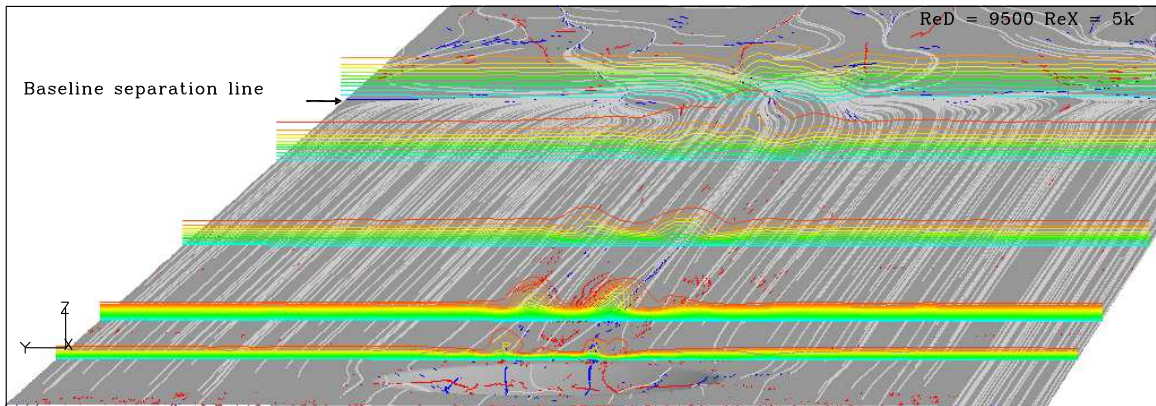


Figure 4.28: Downstream look at contours of u-velocity for $Re_D = 9500$ $Re_x = 5000$. Top contour represents u_{edge}

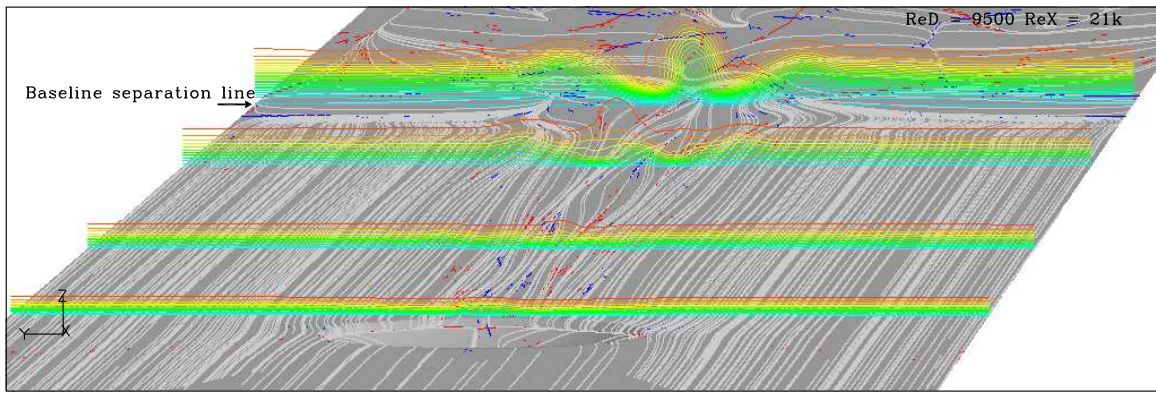


Figure 4.29: Downstream look at contours of u-velocity for $Re_D = 9500$ $Re_x = 21000$. Top contour represents u_{edge}

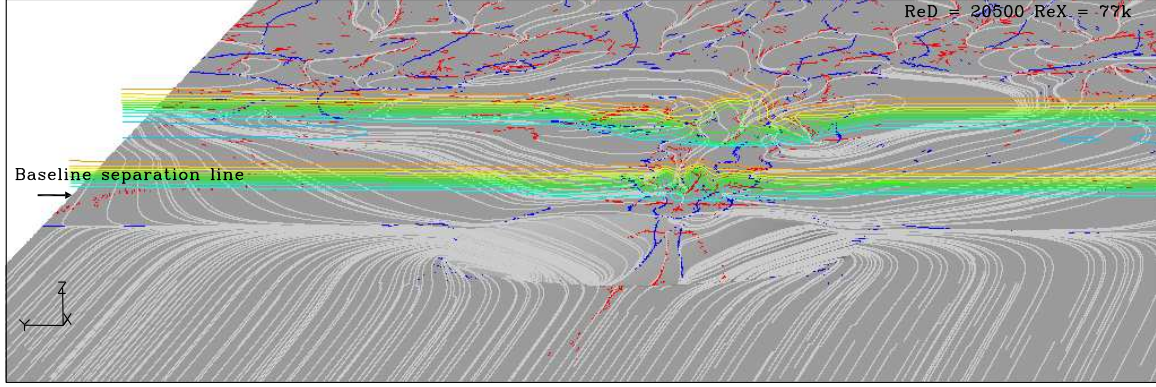


Figure 4.30: Downstream look at contours of u -velocity for $Re_D = 20500$ $Re_x = 77000$. Top contour represents u_{edge}

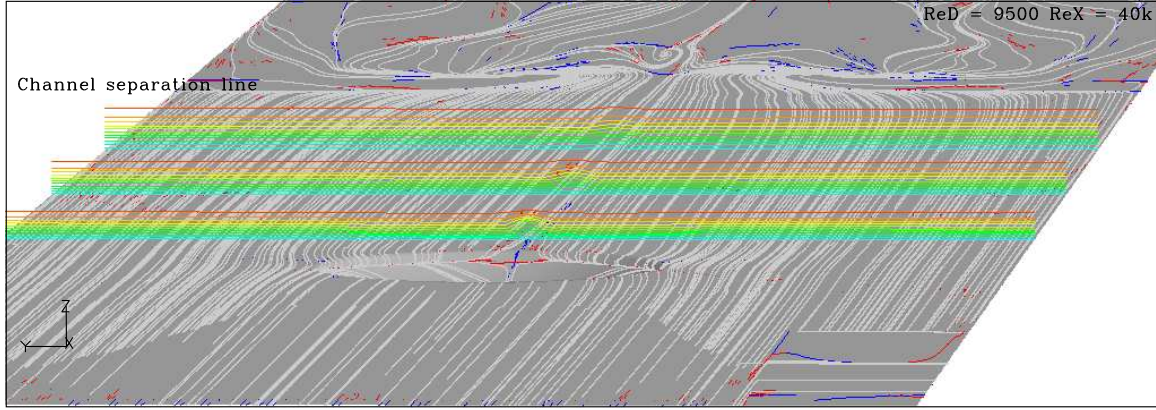


Figure 4.31: Downstream look at contours of u -velocity for $Re_D = 9500$ $Re_x = 40000$. Top contour represents u_{edge}

The transitional energy cases show much less significant downstream effects. Figure 4.30 does, however, seem to depict the flow remaining attached along the centerline beyond the baseline channel separation line. The other transitional case, shown in Fig. 4.31 shows very little effect on the flow. The oil flow does depict the flow staying attached a small distance beyond the baseline channel separation line, but it is a very small improvement.

The low energy cases exhibited little tangible effect down stream at all. Figure 4.32 shows just how little perturbation the dimple inputs into the flow in this low energy regime.

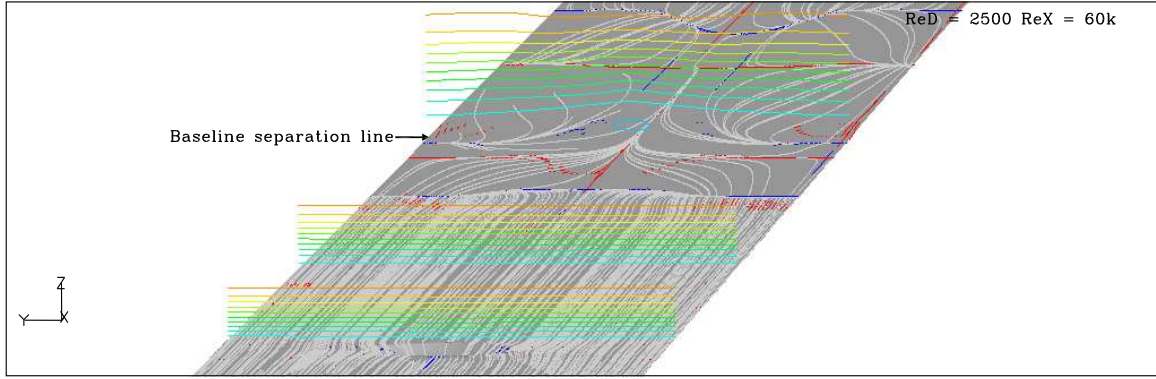


Figure 4.32: Downstream look at contours of u-velocity for $Re_D = 2500$ $Re_x = 60000$. Top contour represents u_{edge}

V. Conclusions

5.1 *Conclusions*

The flow character of the dimple depends primarily on the energy flow into it, as well as the surface interface area between the recirculation zone and the free steam. These two parameters, together, compose the major elements at work in the dimple. The dimple that has the highest energy flow structure has the largest span of the highest energy boundary layer — the large dimple closest to the inlet. Additionally the interface area is also very large which gives opportunity for the flow velocity to catch the vortex structure, and at a high frequency pull it down stream before it can stabilize. At a lower frequency, the dimple tends to 'breathe,' causing the pinned ends to walk in circles around their respective pin points. This movement periodically moves the entire vortex into the more vulnerable high energy wake region in the middle of the dimple and causing the pinned ends to shed. This relationship, though straight forward, does not have a tangible relationship to the higher shedding frequency.

On the other end of the spectrum, when the interface area is low enough, even the highest energy boundary layer inflow does not break the internal vortical structure free from their pin points. At the extreme low energy end, the vortex was sufficiently strong to grow the recirculation zone outside of the dimple and create a separation bubble almost four times the area of the original dimple.

The real benefits of the dimple are seen when the high speed shedding exists. The additional augmentation of the bulk flow shedding of the higher energy spectrums is nearly imperceptible in the down stream and flowfield measurements. Though the lower energy trapped vortex structures have proven to have some benefit [2], the potential benefit of their presence is not maximized without the formation of the fluctuating structures and the shedding of vortices to mix the flow.

5.2 *Recommendations for future research*

The first follow-on research ought to be on more refined and larger grids that allow for feedback on the down-stream results utilizing -DES, LES or DNS solvers. This would require some major changes. First of all, the grid spacing would need to be much tighter in the lateral spacing, even approaching the spacing required vertically for good boundary layer capture. Secondly, the inviscid wall boundary would need to be traded out for a farfield condition with an enforced static pressure gradient. If making a pseudo-farfield condition is not possible, then the follow-on study ought to set the inviscid wall boundary much greater distance (x10) away from the bottom surface, such that a free stream value may be assumed to capture δ^* at some small percentage of the overall height of the channel, and H , θ , and δ_{99} could then be calculated.

More test cases involving variations in the dimple depth at the h/D ratios of (0.075, 0.1, 0.125, 0.15, 0.175, 0.2) would also be interesting. Such an investigation would show the relationship of the dimple volume to the shedding frequency, the vortex stability and the skin friction coefficient.

Another telling study would be to look into elliptical configurations with stream-wise major axis, spanwise major axis, and a set up with the major axis at some angle to the free stream flow. These configurations would help to characterize the importance of the cross flow area and/or dimple volume on the flow structure and the recirculation zone size. Additionally, an elliptical dimple in a slanted configuration could make it possible to generate a sustained streamwise vortex while maintaining the benefits of a recessed vortex generating feature.

When thinking of the downstream effectiveness, it is important to think in terms of the dimple and its ability to induce vortices that can stir the flow and cause the mixing that is desired for the boundary layer attachment problem. This could be reduced to an elementary residence time for the flow over the dimple as simple as a diameter based velocity, or it could involve more complex relationships involving

the flow diffusion time and the characteristics of the flow. An investigation into the non-dimensional parameters to properly characterize the time parameters and their relationships also ought to be accomplished.

Appendix A. Case Specific Data

Tables A.1 through A.3 summarize and list the details mentioned in the above text organized by flow case. this case by case look at the dimples and their characteristics will go in order of decreasing Re_D for all Re_x .

Table A.1: Data reduced from $Re_D = 20500$ cases.

$Re_D = 20500$	$Re_x = 5k$	$Re_x = 66k$	$Re_x = 77k$
Position of pinned vortices from center	x = 42.8%D y = 32%D	x = 41.1 %D y = 27.4%D	x = 45.1%D y = 27.4 %D
Length of pinned vortices	33.4%D	29.1 %D	44.3%D
Average angle	31.3	33.0	35.3
Wake	x = 23%D y = 63%D	x = 23.7 %D y = 38.6%D	x = 8.4%D y = 17.3%D
Frequency	High = 470hz Low = 13hz	High = 480hz Low = 3.96hz	High = 500hz Low = 11.9hz
Strouhal number	1.41	1.47	1.55
St	.13	.12	0.04
Note : Time Averaged Data			

Table A.2: Data reduced from $Re_D = 9500$ cases.

$Re_D = 9500$	$Re_x = 5k$	$Re_x = 21k$	$Re_x = 40k$	$Re_x = 87k$
Position of pinned vortices from center	x = 38.9%D	x = 40.0%D	x = 40.8%D	x = 43.2%D
	y = 38.4%D	y = 37.3%D	y = 33.0%D	y = 29.7%D
Length of pinned vortices	11.9%D	18.7 %D	33.8%D	29.4%D
Average angle (degrees)	43.6	45.2	41.7	36.2
Wake	x = 52.7%D	x = 47.6%D	x = 33.8%D	x = 56.7%D
	y = 60.0%D	y = 46.3%D	y = 21.3%D	y = 0.73%D
Frequency	High = 240hz	High = 282hz	High = 253hz	High = 0hz
	Low = 19.2hz	Low = 0hz	Low = 0hz	Low = 0hz
Strouhal number	0.31	0.37	0.35	0
	0.02	.0	0	0
Note : Time Averaged Data				

Table A.3: Data reduced from $Re_D = 2500$ cases.

$Re_D = 2500$	$Re_x = 5k$	$Re_x = 60k$	$Re_x = 95k$
Position of pinned vortices from center	x = 47.8%D y = 35.1%D	x = 53.1%D y = 26.9%D	x = 42.7%D y = 46.5%D
Length of pinned vortices	35.9%D	27.6%D	54.1%D
Average angle (degrees)	56.0	55.4	49.9
Wake	x = 44.4%D y = 0	x = 54.1%D y = 0	x = 29.4%D y = 0
Frequency	High = 0hz Low = 0hz	High = 0hz Low = 0hz	High = 0hz Low = 0hz
Strouhal number	0 0	0 0	0 0
Note : Time Averaged Data			

Bibliography

1. Bearman P. and Harvey J. "Golf Ball Aerodynamics," *Aeronautical Quarterly*, 27(2):112–122 (April May 1976).
2. Casey J. P. *Effect of Dimple Pattern on the Suppression of Boundary Layer Separation on a Low Pressure Turbine Blade*. MS thesis, Graduate School of Engineering, Air Force Institute of Technology (AETC), Wright-Patterson AFB OH, March 2004. AFIT/GAE/ENY/04-M05.
3. Fluent Incorporated . *User's Guide* (6.2.2 Edition). Fluent Inc., Lebanon, NH, January 2005.
4. Gromov P., Zobnin A., Rabinovich M., and Sushchik M. "Creation of solitary vortices in flow around shallow depression," *Pis'ma v Zhurnal Technicheskoi Fiziki*, 12(21):1323–1328 (1986).
5. Hiwada M., Kawamura T., and Mabuchi . "Some characteristic of flow pattern and heat transfer past a circular cylindrical cavity," *Bulletin of JSME*, 26(220):196–203 (March-April 1983).
6. Intelligent Light . *Fieldview Reference Manual* (10 Edition). Intelligent Light, Lyndhurst, NJ, November 2001.
7. Isaev S. A. and Leont'ev A. I. "Numerical Simulation of Vortex Enhancement of Heat Transfer under Conditions of Turbulent Flow Past a Spherical Dimple on the Wall of a Narrow Channel," *High Temperature (Teplofizika Vysokikh Temperatur)*, Vol. 41, No. 5,(0018-151X/03/4105):755–770 (May 2003).
8. Isaev S. A., Leont'ev A. I., Baranov P. A., Metov K. T., and Usachov A. E. "Numerical Analysis of the Effect of Viscosity on the Vortex Dynamics in Laminar Separated Flow Past a Dimple on a Plane with Allowance for its Assymetry," *Journal of Engineering Physics and Thermophysics (Inzhenerno-Fizicheskii Zhurnal)*, 74, No. 2(UDC 532.517.2):62–77 (March-April 2001).
9. Khalatov A. "Vortex Technologies in Aerospace Engineering." *Proceedings of the U.S. - Ukrainian Workshop "Innovative Combustion and Aerothermal Technologies in Energy and Power System"*. 35–51. May 2001.
10. Khalatov A. and Byerley A. "Flow Characteristics Within and Downstream of a Single and Double Array of Shallow Spherical and Cylindrical Dimples." *Proceedings from ASME Turbo Expo 2006*. 11. Barcelona, Spain: ASME, May 2006. accepted and planned to publish.
11. Khalatov A., Byerley A., Seong-Ki M., and Ochoa D. "Laminar Flow Characteristics in Water Tunnel Within and Downstream of Spherical and Cylindrical Dimples on a Flat Plate." *Proceedings from ASME Turbo Expo 2004*. 2004.

12. Khalatov A., Byerley A., and Vincent R. "Laminar Flow Characteristics in Water Tunnel Within and Downstream of Spherical and Cylindrical Dimples on a Flat Plate." *Proceedings from ASME Turbo Expo 2004*. 2004.
13. Kiknadze G., Krasnov Y., Podymako V., and Khabensky V. *Self-organization of Vortex Structures in a Water Flow Inside Hemispherical Dimples*. Technical Report 291.pp.17-20, Russia: Russian Academy of Sciences, 1986.
14. Lake J., King P., Rivir P. I., and B R. "Low Reynolds number loss reduction on turbine blades with dimples and V-grooves." *38th AIAA Aerospace Sciences Meeting and Exhibit*. January 2000.
15. Lake J. P. *Flow Separation Prevention on a Turbine Blade in Cascade at Low Reynolds Number*. PhD dissertation, Air Force Institute of Technology (AETC), June 1999. AFIT-DS-ENY-99-01.
16. Lavrent'ev M. and Shabat B. *Problems of Hydrodynamics and Mathematical Models* (First Edition). Moscow, Russia: Nauka, 1977.
17. Ligrani P. M., Harrison J. L., Mahmmud G. I., and Hill M. L. "Flow structure due to dimple depressions on a channel surface," *American Institute of Physics*, 13(11):3442–3451 (November 2001).
18. Moon S. and Lau S. "Turbulent Heat Transfer Measurements on a Wall with Concave and Cylindrical Dimples in a Square Channel." *Proceedings From ASME 2002 Conference*. 2002. GT2002-30208.
19. R.Haimes and Kenwright D. "On the Velocity Gradient Tensor and Fluid Feature Extraction," (99-3288) (1999).
20. Rouser K. P. *Use of Dimples to Suppress Boundary Layer Separation on a Low Pressure Turbine Blade*. MS thesis, Graduate School of Engineering, Air Force Institute of Technology (AETC), Wright-Patterson AFB OH, December 2002. AFIT/GAE/ENY/02-13.
21. Sujuki D. and Haimes R. "Identification of Swirling Flow in 3-D Vector Fields," (95-1715) (1995).
22. Syred N., Khalatov A., Kozlov A., Shchukin A., and Agachev R. "Effect of Surface Curvature on Heat Transfer and Hydrodynamics Within a Single Hemispherical Dimple," *Journal of Turbomachinery*, 123(5):609–613 (July 2001).
23. Terekhov V., Kalinina S., and Mshvidobadze Y. M. "Flow structure and heat transfer on a surface with a unit hole depression," *Russian Journal of Engineering Physics*, (5):196–203 (1996).
24. Terekhov V., Kalinina S., and Mshvidobadze Y. "Flow Structure and Heat Transfer on a surface With a Unit Hole Depression," *Russian Journal of Engineering Physics*, (5) (April 1995).

25. Wighart K. "Characterizing the Coefficient of Friction of Turbulent Flow over the Suction Side of Airfoils Erhöhung des Turbulenten Reib-ungswiderstandes Durch Oberflächen-Störungen," *Forschungshefte für Schiffstechnik*, (1):65–81 (April 1953).

REPORT DOCUMENTATION PAGE				Form Approved OMB No. 074-0188	
<p>The public reporting burden for this collection of information is estimated to average 1 hour per response, including the time for reviewing instructions, searching existing data sources, gathering and maintaining the data needed, and completing and reviewing the collection of information. Send comments regarding this burden estimate or any other aspect of the collection of information, including suggestions for reducing this burden to Department of Defense, Washington Headquarters Services, Directorate for Information Operations and Reports (0704-0188), 1215 Jefferson Davis Highway, Suite 1204, Arlington, VA 22202-4302. Respondents should be aware that notwithstanding any other provision of law, no person shall be subject to a penalty for failing to comply with a collection of information if it does not display a currently valid OMB control number.</p> <p>PLEASE DO NOT RETURN YOUR FORM TO THE ABOVE ADDRESS.</p>					
1. REPORT DATE (DD-MM-YYYY) 23-03-2006		2. REPORT TYPE Master's Thesis		3. DATES COVERED (From – To) 22 Aug 2004 – 23 March 2006	
4. TITLE AND SUBTITLE CFD Investigation of the Flow Dynamics Inside a Spherical Surface Indentation				5a. CONTRACT NUMBER	
				5b. GRANT NUMBER	
				5c. PROGRAM ELEMENT NUMBER	
6. AUTHOR(S) Vincent, Robert C., 2 nd Lieutenant, USAF				5d. PROJECT NUMBER	
				5e. TASK NUMBER	
				5f. WORK UNIT NUMBER	
7. PERFORMING ORGANIZATION NAMES(S) AND ADDRESS(S) Air Force Institute of Technology Graduate School of Engineering and Management (AFIT/EN) 2950 Hobson Way WPAFB OH 45433-7765				8. PERFORMING ORGANIZATION REPORT NUMBER AFIT/GAE/ENY/06-M31	
9. SPONSORING/MONITORING AGENCY NAME(S) AND ADDRESS(ES) Un-sponsored				10. SPONSOR/MONITOR'S ACRONYM(S)	
				11. SPONSOR/MONITOR'S REPORT NUMBER(S)	
12. DISTRIBUTION/AVAILABILITY STATEMENT APPROVED FOR PUBLIC RELEASE; DISTRIBUTION UNLIMITED.					
13. SUPPLEMENTARY NOTES					
14. ABSTRACT This study aims to identify the flow structure inside and around a dimple surface indentation that passively reduces flow separation, and to generate characterization parameters for the effectiveness of the aforementioned flow structure in boundary layer separation control. In this study the surface indentation is cut into a flat plate in a diverging channel that creates an adverse pressure gradient. In the baseline flat plate conditions, the shedding vortices formed by the pressure gradient create an oscillating pressure field in the dimple. This geometry has been chosen to simulate the adverse pressure gradient present in the flow regime found on a turbine blade experiencing flow separation, while at the same time reducing overall computational cost. The flow regimes studied range from Re_D of 2500 to 20500 (by varying the dimple size) and at various boundary layer thicknesses Re_x from 5000 to 80000 (by changing the dimple flow wise location) based on proximity to the base-line separation point. The points of interest verified and closely monitored are the vortical structures inside the dimple and their down stream effects.					
15. SUBJECT TERMS Turbine blades, Boundary layer control, Flow separation, vortex generators					
16. SECURITY CLASSIFICATION OF:			17. LIMITATION OF ABSTRACT	18. NUMBER OF PAGES	19a. NAME OF RESPONSIBLE PERSON
REPORT	ABSTRACT	c. THIS PAGE			Maple, R., LtCol, USAF
U	U	U	UU	79	19b. TELEPHONE NUMBER (Include area code) (937) 255-3636, ext 4577; raymond.maple@afit.edu